

# We are IntechOpen, the world's leading publisher of Open Access books Built by scientists, for scientists

6,300

Open access books available

171,000

International authors and editors

190M

Downloads

Our authors are among the

154

Countries delivered to

TOP 1%

most cited scientists

12.2%

Contributors from top 500 universities



WEB OF SCIENCE™

Selection of our books indexed in the Book Citation Index  
in Web of Science™ Core Collection (BKCI)

Interested in publishing with us?  
Contact [book.department@intechopen.com](mailto:book.department@intechopen.com)

Numbers displayed above are based on latest data collected.  
For more information visit [www.intechopen.com](http://www.intechopen.com)



---

# Introductory Chapter: Genome of Material for Combinatorial Design and Prototyping of Alloys

---

Igor Shishkovsky

Additional information is available at the end of the chapter

<http://dx.doi.org/10.5772/intechopen.77360>

---

## 1. Material genome: New paradigm of additive manufacturing

Materials present an integral part of the additive technology (AT). The key task in creation and processing of new materials for the AT is to expand the range of such materials (including through mixing/alloying/modeling of composites), to improve their quality, to increase the additive process stability, reproducibility and reliability, including by using multimaterial powdered systems, while maintaining a low cost of materials, the process of their manufacturing and pre- and/or post-processing.

However, the development of the AT components (i.e., technologies and equipment for the powdered material manufacturing, 3D part synthesis and subsequent post-processing) without a concurrent improvement of the accompanying directions does not allow obtaining the maximum effect. The conventional cycle of the development of new materials for the additive manufacturing (AM) transition needs a revision.

In 2011, the administration of President Obama presented two breakthrough initiatives, “MGI—Material Genome Initiative for Global Competitiveness” and “AMP—Advanced Manufacturing Partnership,” prepared by the USA National Council for Science and Technology [1, 2]. In the AT literature, the second initiative is mostly mentioned. Indeed, the AMP allowed the launch of a number of projects in the USA: America Makes—National Additive Manufacturing Innovation Institute (NAMII); Lightweight and Modern Metals Manufacturing Innovation (LM3I) Institute; Digital Manufacturing and Design Innovation (DMDI) Institute [3–5]. Nevertheless, the MGI initiative is no less significant. In fact, it is a set of tools that implement the iterative concept of the new material development, which allows reducing of the resource intensity (time and cost) of the material science cycle by 50% [1]. The essence of the concept consists of a continuous exchange of information at different stages of the development of

new materials, not only within a single subject area (e.g., structural or functional materials), but for all the types of materials (**Figure 1**).

Along with the “America Makes” additive community [3], a self-regulating society has been formed in the United States that consolidates scientists engaged in the development and commercialization of new materials based on the MGI concept [1]. The accumulation of information (Big Data (BD)), presentation of tools for their use and creation of other tools provide a transition from quantity to quality. The principles of open architecture provide the concentration of new ideas in the MGI community. The use of block-chain technologies [6] allows ensuring of the MGI implementation under the BD using, provides the data management, guarantees their reliability and significantly improves quality due to the internal certification of future 3D AM parts.

The traditional cycle of the new material fabrication includes the following stages: (1) development of the material composition; (2) optimization of the material properties; (3) design of products from the material, including manufacturing techniques; (4) testing and certification of the material; (5) commercialization of the material.

The iterative cycle proposed within the framework of the MGI concept allows to combine separate stages in different directions so that to accelerate the achievement of the results (see **Figure 1**). In particular, the information about materials, about the AM processes and optimal regimes for the 3D parts fabrication is subject to association. On the other hand, the spatial and temporal scalability of modern methods of computational materials science should be combined with the experimental results under the searching of optimal AM regimes, that is, should find the experimental confirmation.

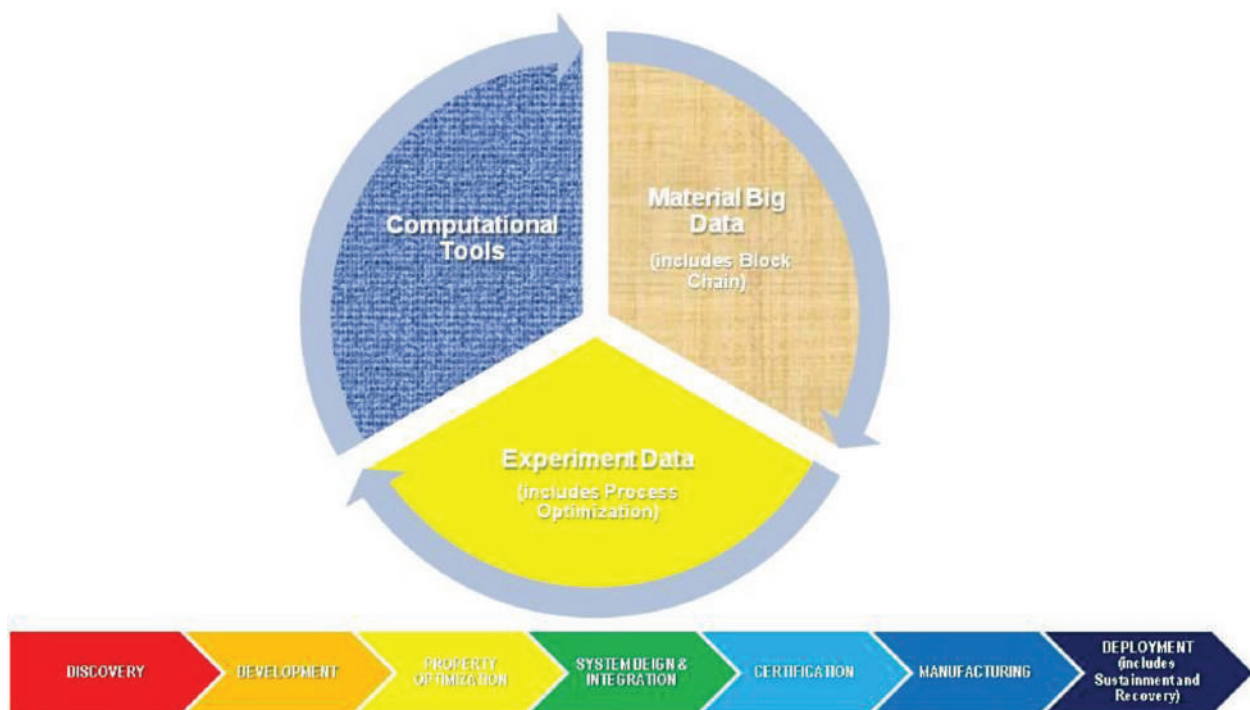


**Figure 1.** Additive manufacturing via material genome route.

The MGI concept emergence became possible due to the advanced achievements in the information technologies (IT) over the past 10 years, namely, due to the cost reduction of the information transmission and storage, increase of the speed of transmission and processing of the information. Priority MGI trends in the AM applications are

- optimization of the development technologies for the complex high-dimensional phase spaces;
- effective methods for the experimental data analysis in order to determine the relationship between properties of different levels (e.g., between microstructure, chemical composition, processing and volume properties);
- fundamental properties of the materials behavior;
- tools for experimental data analyzing and the relationship between the experimental data and predictive modeling;
- revision of theories, modification and updating of the developed models and methods, realization of new experiments, caused by the discrepancy between the theory and new experimental data and modeling.

The MGI approaches erase boundaries between a wide range of materials both in the areas where numerical methods are already in use—structural materials, including composites, and also in the areas where they are still weakly used, for instance for soft materials (oligomers, polymers, 3D inks-jet, powders, wires, etc.).

The essence of the approaches used in MGI can be understood on the basis of the MGI Principal Investigator Meeting projects of the first and second wave conducted in the USA in 2015–2016 [7, 8].

## 2. MGI in high-performance metals and alloys

The MGI approaches are actively applied both in the development of structural materials and for manufacturing technologies. Depending on the property being modeled, object and process, the following levels are distinguished: atomic, micro, meso- and macrolevels, and the conditional size ranges are  $<A$ -nm, nm- $\mu$ m,  $\mu$ m-mm,  $>$ mm, respectively. For each level, certain modeling methods are characteristic.

Atomic modeling is widely used in developing new materials and predicting their features. Here, the numerical molecular dynamics models as well as the density functional theory are used.

At the micro level, the data on the phase stability are determined as the input data for thermodynamic models used to calculate the phase diagrams and crystallization points.

The problems solved by meso-level modeling lie on the border of micro- and macrolevels. There is practically no commercial software for meso-level modeling, still a large number

of user subprograms have been developed that extend the resource of standard computing packages. For this, the computational methods are used such as the phase field model, discrete dislocation dynamics, physical plasticity theory, and so on.

At the macrolevel, the problems of mechanics of continua are solved by using the finite elements methods (FEM) and finite differences method (FDM). Recently, an actively developed approach is that involving the creation of structural and multi-physical models based on the FEM [9].

It is obvious that the possibilities for the MGI use should most clearly reveal themselves in the AT, since in fact these technologies are digital manufacturing. The technologies of direct and layerwise laser additive manufacturing (LAM) make it possible to obtain products with directional anisotropy due to their ability to control the laser beam trajectory during fusion and to determine technological parameters such as laser beam diameter, linear energy density and scanning geometry. The 3D part fabrication with the areas differing by their characteristics depending on the local loading conditions becomes possible through the use of technologies of a direct laser deposition (DLD). The ability to design the topology of the macrostructure of the synthesized material is one of the main advantages of the AT in the framework of the concept for generating of smart materials. At the same time, the fused particles arrangement and their size are largely stochastic, thus leading to the material structural heterogeneity and the emergence of defects in the form of residual porosity. In addition, despite the application of the technique of the repeated remelting of the surface layer, the resulting roughness does not meet the engineering requirements. In this connection, there exist the following widespread post-processing methods for the synthesized parts that are divided into two types of technologies—volume effect technologies (hot isostatic pressing (HIP) and surface effect technologies)—that include finishing mechanical (or abrasive) treatment, electrophysical and electrochemical techniques, methods for surface layer modification. A particular attention should be paid here to the methods for predicting of the finished parts properties, taking into account their heterogeneity, as well as to the methods for correction of these properties, for example, by modifying the surface layer of products.

The development and use of the MGI methods in the AT design will improve the predicting accuracy of the material properties and of the surface layer of the parts after modification. The influence on the texture and structure will allow to form the properties of finished parts, not only in the obvious area of the surface layer microhardness increase, but also in providing an enhanced corrosion and erosion resistance; and crack resistance owing to the formation of compression stresses.

The Material Genome Initiative (MGI) offers a paradigm that perfectly matches the AM needs. The MGI is built on the base of the search of specific materials that ensure the generation of different final properties via using different processes. It connects multiple scales, from quantum and atomistic to molecular mechanics and derived potentials, mesoscale (nanometer) methods and, finally, continuum methods. The characteristics and effects of the process play an integral role in the material genome (MG). A similar approach for combining the scales and methods is suitable for the AM. In the AM, the material microstructure can be adapted to the specific requirements and needs, thus providing wide possibilities for the material design.

For AT, the problems of certification and safety of the used powder materials and the received 3D products are especially relevant, since these products can work in the important mechanisms of perspective modern cars, aircrafts or missiles. Therefore, the developed approaches for the selection and storage of the data on materials and/or processes are of an extreme necessity. The monitoring of the storage conditions of all the data, codes, and discussions with graphically attached persistent identifiers, along with the low maintenance costs, is fundamental to the continuous and efficient complex operation of the whole platform.

The digital recording of code and data transformations that occur among users of the platform during their cooperative work provides new rich opportunities capable of improving the integration and operational process in all directions (including research, education, authentic knowledge transfer, manufacturing and product life cycle).

### 3. Combinatorial design of alloys for AM

A wide range of the AM materials and processes requires extensive researches and determination of the “process-structure-properties” relationships. For fabrication of unique structures that do not exist in nature or reproduce its best manifestations (e.g., the parts with a negative coefficient of thermal expansion or optical transmission), of metamaterials, biomimetic structures and surfaces, the problems of using the unique AT resource are of no less interest. Besides, one should also realize the AT applicability for the manufacturing of materials with multilevel hierarchical functionality on nano-, micro- and mesoscales, up to the development of the 3D-printing tools for fabrication of atom-by-atom structures and construction of additive nanofabricators [10].

The 3D combinatorial metallurgical method, called a “*Rapid Alloy Prototyping*” (RAP), has been recently proposed by Prof. D. Raabe with coworkers [11] and showed a successful testing on Twinning-Induced Plasticity (TWIP) steels with reduced density [12, 13], high-entropy alloys [14–16], intermetallic alloys [17, 18], high-strength martensitic [19, 20] and high-modulus steels [21]. It includes semicontinuous high-performance fabrication of the 3D parts, their heat treatment, preparation to testing, allowing to synthesize and test up to 45 material parameters within 35 h [11].

The ideas of the LAM use for fabrication of both functional and gradient alloys (FG) have been discussed for a long time [22–24]. However, in the combinatorial design of alloys by the RAP method, the LAM use provides a number of additional advantages.

First, a specific thermal regime is realized throughout the metallurgical process [25, 26]: the temperature-time profile for the samples obtained by LAM methods is rather different from those observed in a typical metallurgical manufacturing. Under layer-by-layer (3D) laser cladding, the powder material is quenched after the melting and crystallized at high speeds due to a rapid heat removal to the substrate. With the overlay of each following layer during the subsequent layers cladding, the consolidated material is repeatedly heated and even melted partially by a laser beam [25, 26]. This means that the materials produced by the LAM are subjected to a series of consecutive short-pulse temperature cycles of a decreasing intensity [25, 27]. Such cyclic heat treatment can also be used for controlling of solid-phase transformations in

the material after the cladding. This is favorable for structural steels and super-alloys where the strength, toughness and hardness are ensured by the dispersion hardening also [17].

The second advantage of the LAM use for combinatorial development of high-performance alloys is that a rapid melting and solidification occur locally, within a small volume [25, 26]. This allows working with the materials that are not melting or hardly melting in an ingot, for example, oxide-strengthened alloys, or materials containing components in the amount exceeding the solubility limit in the solid solution. Typical cooling rates for the LAM are from  $10^3$  to  $10^6$  K/s [25, 26]. These high cooling speeds lead to a rapid solidification of the melt, creation of a finely dispersed structure that increases plasticity, in contrast to the coarse-grained cast structure obtained by a continuous casting [25, 27]. This proves that the LAM can serve not only as an instrument for combinatorial alloy modeling, but also ensures a qualitative expansion of options for the additive manufacturing (AM).

Third, some LAM methods are “self-adapted” for the RAP, that is, they quickly outline suitable series of applicable compositions, which is explained by the peculiarities of powder metallurgy as a production process [10, 25, 26].

For the RAP purposes, from the whole scope of the AT variety, layer-by-layer selective laser melting (SLM) or laser metal deposition (LMD) techniques can be recommended [28]. The latter is sometimes also referred to as 3D-laser-cladding (or direct metal deposition—DMD) & Laser Engineered Net Shaping (LENS). Thus, all the above said characterizes the LAM as a highly effective technology for the fast study and development of new alloys and the 3D part manufacturing on their basis.

## 4. Conclusion

The aim of this introductory chapter is to designate for the readers of this monograph the vector of development of these two approaches—the MGI and the newest methodology for rapid alloy prototyping (i.e., accelerated development and testing of new alloys) based on the combination of LAM technologies and methods of combinatorial design. The presentation pursued three goals:

- the first goal was to represent the efficiency of the combination of these two approaches for accelerated manufacturing (i.e., RAP) and study of the alloy versions;
- the second goal was to determine the compositions of the selected composite alloys, providing improved properties in comparison with the existing analogues;
- the third goal was to determine and demonstrate the possibility (in-situ, i.e., on-site) of obtaining metal parts with a pre-specified heterogeneity of microstructure and properties.

The last goal is the most significant for high-performance structural alloys, since the products made of them often must combine a high hardness of the surface layer with a softer and viscous core. The LAM is obviously a technology that is most fitted for a systematic study of all these aspects and provides the possibility of creating complex parts based on digital models using the selected powder compositions. It was noted that:

1. The new concept, Material Genome, allows consolidating the efforts aimed to develop such directions as “new materials,” “computer technologies for modeling and production of parts” and “additive manufacturing” by providing a single tool that helps to achieve breakthrough results by applying new methods and approaches.
2. The DMD and SLM are suitable for obtaining of 3D samples with a constant or variable composition of the material and can be used for combinatorial design and development of new alloys. The LAM allows the creation of compositionally piecewise-continuous gradient materials and obtainment in situ of new alloys that are not necessarily made from pre-prepared metal powders and is an effective tool for the rapid development of a new alloy. An additional advantage of the DMD in comparison with the SLM in the context of combinatorial metallurgical synthesis is high cladding rates and large dimensions of 3D parts, which are not limited by the dimensions of the synthesis chamber in the SLM installation.
3. Equally important is the possibility to obtain with the aid of the LAM, compositions and microstructures of alloys that are not available for traditional technologies. This principle feature can be used as a goal of combinatorial development of unique alloys for the LAM. It should also be noted that with the DMD, a gradient sample comprising parts from different alloys can be subjected to the HIP (post-treatment) and further research of the alloys that are changing in their composition from the viewpoint of their behavior during the thermo-mechanical treatment.

## Author details

Igor Shishkovsky

Address all correspondence to: [shishkovsky@gmail.com](mailto:shishkovsky@gmail.com)

Lebedev Physics Institute of Russian Academy of Sciences, Samara, Russian Federation

## References

- [1] Materials Genome Initiative for Global Competitiveness. Available from: [https://www.mgi.gov/sites/default/files/documents/materials\\_genome\\_initiative-final.pdf](https://www.mgi.gov/sites/default/files/documents/materials_genome_initiative-final.pdf) [June 24, 2011]
- [2] President Obama Launches Advanced Manufacturing Partnership. Available from: <https://www.nist.gov/news-events/news/2011/06/president-obama-launches-advanced-manufacturing-partnership> [June 24, 2011]
- [3] America Makes—National Additive Manufacturing Innovation Institute (NAMII) Available from: <https://www.americamakes.us/>
- [4] The Lightweight Modern Metals Manufacturing Institute—NIST. Available from: [https://www.nist.gov/sites/default/files/documents/el/msid/18\\_1Brown.pdf](https://www.nist.gov/sites/default/files/documents/el/msid/18_1Brown.pdf)
- [5] Digital Manufacturing and Design Innovation Institute—UI Labs. Available from: <http://www.uilabs.org/innovation-platforms/manufacturing/>

- [6] Industry 4.0 Challenges and solutions for the digital transformation and use of exponential technologies. Deloitte—Audit. Tax. Consulting. Corporate Finance. Available from: <https://www2.deloitte.com/content/dam/Deloitte/ch/Documents/manufacturing/ch-en-manufacturing-industry-4-0-24102014.pdf>
- [7] 2nd Annual Principal Investigator Meeting. Accelerating Materials Research, Meeting Societal Needs, Building Infrastructure for Success. DOE/NSF Materials Genome Initiative. Bethesda, MD; 12-13 January 2015. Available from: [https://www.mgi.gov/sites/default/files/documents/2015\\_MGI\\_PI\\_Meeting\\_Abstract\\_Book.pdf](https://www.mgi.gov/sites/default/files/documents/2015_MGI_PI_Meeting_Abstract_Book.pdf)
- [8] Third Principal Investigator Meeting. Accelerating Materials Research. Materials Genome Initiative. Available from: [https://www.mgi.gov/sites/default/files/documents/2016\\_Abstract\\_Book\\_Final.pdf](https://www.mgi.gov/sites/default/files/documents/2016_Abstract_Book_Final.pdf)
- [9] Modeling Across Scales: A Road mapping Study for Connecting Materials Models and Simulations Across Length and Time Scales. Available form: [http://www.tms.org/portal/PUBLICATIONS/Studies/Modeling\\_Across\\_Scales/portal/Publications/Studies/Modeling\\_Across\\_Scales.aspx](http://www.tms.org/portal/PUBLICATIONS/Studies/Modeling_Across_Scales/portal/Publications/Studies/Modeling_Across_Scales.aspx)
- [10] Shishkovsky Igor V, editor. New Trends in 3D Printing. Rijeka, Croatia: InTech Publish.; 2016. 268 p. ISBN: 978-953-51-2480-1. (Open access)
- [11] Knoll H, Ocylok S, Weisheit A, et al. Combinatorial alloy design by laser additive manufacturing. *Steel Research International*. 2017;**88**:1600416. DOI: 10.1002/srin.201600416
- [12] Springer H, Raabe D. Rapid alloy prototyping: Compositional and thermo-mechanical high throughput bulk combinatorial design of structural materials based on the example of 30Mn-1.2C-xAl triplex steels. *Acta Materialia*. 2012;**60**:4950-4959
- [13] Raabe D, Springer H, Gutierrez-Urrutia I, et al. Alloy design, combinatorial synthesis, and microstructure-property relations for low-density Fe-Mn-Al-C austenitic steels. *JOM*. 2014;**66**:1845-1856
- [14] Pradeep KG, Tasan CC, Yao MJ, et al. Non-equiatomic high entropy alloys: Approach towards rapid alloy screening and property-oriented design. *Materials Science and Engineering A*. 2015;**648**:183-192
- [15] Li Z, Pradeep KG, Deng Y, et al. Metastable high-entropy dual-phase alloys overcome the strength-ductility trade-off. *Nature*. 2016;**534**:227
- [16] Tasan CC, Deng Y, Pradeep KG, et al. Composition dependence of phase stability, deformation mechanisms, and mechanical properties of the CoCrFeMnNi high-entropy alloy system. *JOM*. 2014;**66**:1993-2001
- [17] Shishkovsky IV, Nazarov AP, Kotoban DV, Kakovkina NG. Comparison of additive technologies for gradient aerospace part fabrication from nickel based superalloys. In: Aliofkhazraei M, editor. *Superalloys*. Rijeka, Croatia: InTech Publ.; 2015. 344 p. DOI: 10.5772/61121

- [18] Shishkovsky IV. Laser controlled intermetallics synthesis during surface cladding. In: Lawrence J et al., editors. *Laser Surface Engineering. Processes and Applications*. Woodhead Publishing. 2014. 718 p. DOI: 10.1016/B978-1-78242-074-3.00011-8
- [19] Springer H, Beide M, Raabe D. Bulk combinatorial design of ductile martensitic stainless steels through confined martensite-to-austenite reversion. *Materials Science and Engineering A*. 2013;**582**:235-244
- [20] Springer H, Belde M, Raabe D. Combinatorial design of transitory constitution steels: Coupling high strength with inherent formability and weldability through sequenced austenite stability. *Materials & Design*. 2016;**90**:1100-1109
- [21] Aparicio-Fernandez R, Springer H, Szczepaniak A, et al. In-situ metal matrix composite steels: Effect of alloying and annealing on morphology, structure and mechanical properties of TiB<sub>2</sub> particle containing high modulus steels. *Acta Materialia*. 2016;**107**:38-48
- [22] Shishkovsky IV. Synthesis of functional gradient parts via RP methods. *Rapid Prototyping Journal*. 2001;**7**(4):207-211
- [23] Collins PC, Banerjee R, Banerjee S, Fraser HL. Laser deposition of compositionally graded titanium-vanadium and titanium-molybdenum alloys. *Materials Science and Engineering*. 2003;**A352**:118-128
- [24] Hofmann DC, Roberts S, Otis R, et al. Developing gradient metal alloys through radial deposition additive manufacturing. *Scientific Reports*. 2014;**4**:5357. DOI: 10.1038/srep05357
- [25] Ian Gibson, David W. Rosen, Brent Stucker. *Additive Manufacturing Technologies; Rapid Prototyping to Direct Digital Manufacturing*; Verlag: Springer US; 2010. ISBN: 978-1-4419-1119-3. <https://www.springerprofessional.de/additive-manufacturing-technologies/1719670>
- [26] Shishkovsky IV. *Fundamentals of Additive Technologies of High Resolution*. Saint-Petersburg: Piter Publ; 2016. 400 p. ISBN: 978-5-496-02049-7 (in Russian)
- [27] Jagle EA, Choi PP, Humbeeck J, Raabe D. Precipitation and austenite reversion behavior of a maraging steel produced by selective laser melting. *Journal of Materials Research*. 2014;**29**(17):2072-2079
- [28] Shishkovsky IV. Combinatorial design of alloys via laser additive technologies. *Stankoinstrument*. 2017;**3**:38-49. DOI: 10.22184/24999407.2017.8.3.38.49 (in Russian)



# We are IntechOpen, the world's leading publisher of Open Access books Built by scientists, for scientists

6,300

Open access books available

171,000

International authors and editors

190M

Downloads

Our authors are among the

154

Countries delivered to

TOP 1%

most cited scientists

12.2%

Contributors from top 500 universities



WEB OF SCIENCE™

Selection of our books indexed in the Book Citation Index  
in Web of Science™ Core Collection (BKCI)

Interested in publishing with us?  
Contact [book.department@intechopen.com](mailto:book.department@intechopen.com)

Numbers displayed above are based on latest data collected.  
For more information visit [www.intechopen.com](http://www.intechopen.com)



---

# A Two-Dimensional Simulation of Grain Structure Growth within Substrate and Fusion Zone during Direct Metal Deposition

---

Jingwei Zhang, Lei Yan, Wei Li and Frank Liou

Additional information is available at the end of the chapter

<http://dx.doi.org/10.5772/intechopen.73107>

---

## Abstract

In this chapter, a predictive multiscale model based on a cellular automaton (CA)-finite element (FE) method has been developed to simulate thermal history and microstructure evolution during metal solidification for direct metal deposition (DMD) process. The macroscopic FE calculation that is validated by the thermocouple experiment is developed to simulate the transient temperature field and cooling rate of single layer and multiple layers. In order to integrate the different scales, a CA-FE coupled model is developed to combine with thermal history and simulate grain growth. In the mesoscopic CA model, heterogeneous nucleation sites, grain growth orientation and rate, epitaxial growth, remelting of preexisting grains, metal addition, grain competitive growth and columnar to equiaxed phenomena are simulated. The CA model is able to show the entrapment of neighboring cells and the relationship between undercooling and the grain growth rate. The model predicts the grain size and morphological evolution during the solidification phase of the deposition process. The developed "decentered polygon" growth algorithm is appropriate for the nonuniform temperature field. Finally, the single- and multiple-layer DMD experiments are conducted to validate the characteristics of grain features in the simulation.

**Keywords:** finite element, cellular automata, grain morphology, direct metal deposition, thermal modeling

---

## 1. Introduction

Compared with the conventional subtractive manufacturing technologies, additive manufacturing (AM) has unique advantages including low heat input, small heat-affected zone, solid-free-form fabrication, near-net-shape and so on. Direct metal deposition (DMD), a rapid developing AM

technique, is able to manufacture a fully dense metal part without intermediate steps, which is especially appropriate for the heterogeneous components manufacturing. During the deposition process, solidification thermodynamics determined by a series of process parameters affect microstructure evolution, which directly affects materials' mechanical properties. The temperature field history and the cooling rate are the key factors to control the solidification microstructure after DMD process [1]. Several approaches, including stochastic and deterministic, have been taken to model solidification microstructure evolution. Anderson and Srolovitz et al. [2, 3] developed a Monte Carlo (MC) stochastic method to simulate the grain growth, grain size distribution, curvature and growth rate as well as their interrelationships. Saito and Enomoto [4] incorporated the anisotropy of the grain boundary energy, the pinning effect of precipitates on growth kinetics into the MC simulation. Another idea of modeling is the deterministic approach. Chen [5] investigated a phase field (PF) method to model and to predict the mesoscale morphological and microstructure evolution in materials. C.E. Krill III, Böttger B, and Moelans N et al. [6–8] developed PF to simulate 2D grain growth, 3D grain growth and equiaxed solidification. However, a phase field model usually carries a very high computational cost because of a requirement for a particularly fine computational grid.

In order to reduce the computational cost, Rappaz and Gandin [9] put forward a 2D cellular automaton approach to model the grain structure formation in the solidification process. The model includes the mechanisms of heterogeneous nucleation and grain growth during the casting process. Nucleation occurring at the solid/liquid interface and the liquid bulk is treated by using different nucleation sites preference. The crystallographic orientation and locations of the grains are randomly selected among a certain number of orientation classes and millions of CA cells, respectively. However, the model was only applied to uniform temperature field. In order to develop the nonuniform temperature prediction, Gandin and Rappaz [10] proposed a 2D cellular automaton (CA) technique for the simulation of grain formation during solidification. The nonuniform temperature situation was fully coupled to finite element (FE) heat flow calculation with enthalpy. This progress made it possible to combine the temperature field history with the microstructure evolution. The coupled CA-FE model is applied to Al-7 wt% Si alloy. A 3D CA-FE model was analyzed for the prediction of dendritic grain structures formed during solidification [11]. The potentiality of the CA-FE model is demonstrated through the predictions of typical grain structures formed during the investment casting and continuous casting processes. Based on the features of several developing approaches, Choudhury et al. [12] compared a CA model with a PF model for dendritic solidification of an Al-4 wt%Cu alloy, 2D and 3D at different undercooling conditions. In 2D case, there is a very good agreement of the simulated tip properties. At high undercooling, the CA model becomes more favorable, as its reproduction of the theoretical behavior is improved. Since the CA model can simulate at coarse scales during a relatively short time, its output can be employed as the input for a PF simulation in order to resolve finer details of microstructure formation within grains. This can be utilized to build a hybrid model to integrate CA high efficiency and PF accuracy. Dore [13] investigated quantitative prediction of microsegregation during solidification of the ternary alloy system, which is applied to solidification of Al-Mg-Si. Jarvis et al. [14] firstly compared 1D, 2D and 3D cellular automaton finite difference (CA-FD) simulations of nonequilibrium solidification in Al-3.95Cu-0.8Mg ternary alloy. It has been demonstrated that there is a good agreement between all the CA-FD models in terms of primary  $\alpha$ -Al phase. However, final dendrite arm spacings of 2D and 3D are slightly overestimated.

High cooling rate and nonequilibrium are typical characteristics of the DMD technique comparing conventional casting process and simulation. Grujicic et al. [15] proposed a modified CA-based method to investigate the evolution of solidification grain microstructure during the LENS rapid fabrication process. This research established the relationship between the process parameters (e.g., laser power, laser velocity) and solidification microstructure in binary metallic alloy. The finite difference analysis was also coupled with the modified CA to calculate the temperature field as the input of microstructure prediction. Kelly and Kampe [16, 17] developed the thermal history in DMD of Ti6Al4V and microstructural characterization. Nie et al. [18] developed a multiscale model to simulate microstructure evolution during laser additive manufacturing solidification. The study presented the relationship between the solidification conditions and the resultant microstructure, especially Laves phase particles in Ni-based superalloy. Rodgers et al. [19] proposed a 2D mesoscale model to simulate grain structure near a moving heat source with kinetic Monte Carlo simulator during electric beam melting (EBM) process. The method is capable of simulating both singlepass and multipass welds grain morphology. It also investigates the influence of initial substrate grain size on HAZ and FZ grain shape and size. Rai et al. [20] coupled a lattice Boltzmann (LB) and cellular automaton (CA) to simulate the microstructure evolution during electron beam melting. Initial grain selection at the base plate, grain boundary perturbation, grain nucleation due to unmolten powder particles in the bulk, grain penetration can all be simulated. The influence of process parameters on the final grain structure and texture evolution is analyzed. Keller et al. [21] investigated aspects of microstructure and microsegregation during rapid solidification in a laser powder bed fusion additive manufacturing process. Finite element analysis is employed to simulate the laser melt pool and temperature field. Microsegregation between dendritic arms is calculated by using the Scheil-Gulliver solidification model and DICTRA software. Phase field is developed to produce microstructures with primary cellular/dendritic arm spacing. However, there are few investigations on microstructure evolution prediction based on substrate and fusion zone during DMD process. Compared to other powder bed additive manufacturing process, there is different thermal cycle and the cooling rates for DMD process, which results in different microstructure. This part-level simulation on microstructure is critical because it provides the foundation for the prediction and control of mechanical properties.

CA simulation is appropriate for mesoscale modeling of grain structure because it does not consider much details inside a specific grain such as secondary dendritic arm spacing (SDAS) and microsegregation. Since it belongs to mesoscale model and does not cost as much computational resources as other microscale models, such as phase field and molecular dynamic, these characteristics of CA model make it appropriate for simulating the part-level grain structure instead of a very small region including less than a hundred grains. Thus, it can be used to predict and control the mechanical properties of the whole part based on the part-level grain structure under different parameters. Molecular dynamic (MD) simulation of microstructural evolution during additive manufacturing [22] is focused on a microscalability, which is between nanometer and micrometer. MD simulation can provide a method to investigate the crystallization process within the HAZ and clarify its crystallization mechanism because it is difficult to observe directly the crystallization process in the HAZ during the cyclic heating and cooling process. Even though MD can investigate microstructure evolution on a molecular level, it will cost too much resource to simulate the whole part structure and properties. PF model [21, 23], a microscopic one, can be used to simulate the solute concentration and phase transformation by solving the potential equation. The coefficients in the evolution equation

of phase-field variables are related to the material parameters so that it can quantitatively simulate grain growth within a finer scale compared to CA and MC. Lattice Boltzmann (LB) method is adopted to numerically simulate the solute transport within the melt pool domain because it is appropriate for the complex geometry shape and is built from the temporal and spatial discretized grid, avoiding solving macroscopic N-S equations. The computational domain is discretized into regular lattices with the same cell size as the CA model. The governing equation and boundary conditions for transport process are described in detail in Refs. [24–27]. The comparison of AM microstructure simulation methods is shown in **Table 1**. The current CAFÉ model can be used to consider multiple components if it considers the solute concentration and there is no chemical reaction and intermetallic phase formation during the solidification process. However, it is not capable of determining the mechanical properties directly if it is not incorporated with other models such as Hall-Petch model.

Methods	Advantages	Limitations
Cellular automaton	<ul style="list-style-type: none"> <li>• Coupled prediction of thermal history and grain structure</li> <li>• Predicts microstructure with multiple heat source passes</li> <li>• Including crystallographic orientation and texture</li> <li>• Relatively low computational cost</li> </ul>	<ul style="list-style-type: none"> <li>• No HAZ grain evolution</li> <li>• Unavailable open source code</li> <li>• Lack of grain substructure</li> </ul>
Monte Carlo	<ul style="list-style-type: none"> <li>• Predicts 3D microstructures with hundreds of heat source passes</li> <li>• Microstructure evolution within fusion zone and HAZ</li> <li>• Included in the open source code</li> </ul>	<ul style="list-style-type: none"> <li>• Idealized molten zone</li> <li>• No direct coupling of thermal and microstructural models</li> <li>• Does not incorporate material texture or anisotropy.</li> </ul>
Phase field	<ul style="list-style-type: none"> <li>• Available subgrain features</li> <li>• Including solute concentration and phase transformation</li> <li>• Material parameters related to phase-field variables</li> </ul>	<ul style="list-style-type: none"> <li>• High computational cost</li> <li>• Small computational domain</li> <li>• Solving complex potential equations</li> </ul>
Lattice Boltzmann	<ul style="list-style-type: none"> <li>• Allows for coupled thermo-fluid and microstructure evolution on same lattice</li> <li>• Including crystallographic orientation and texture</li> <li>• Appropriate for the complex geometry shape</li> <li>• No need to solve macroscopic N-S equations</li> </ul>	<ul style="list-style-type: none"> <li>• Unstable solutions for many regimes</li> <li>• No solid-state grain evolution after solidification</li> <li>• Unavailable open source code</li> </ul>
Molecular dynamics	<ul style="list-style-type: none"> <li>• Explain crystallization mechanism</li> <li>• Simulating microstructure within HAZ</li> </ul>	<ul style="list-style-type: none"> <li>• Costs too much computational resource</li> <li>• Very small computational region</li> </ul>
Empirical microstructure models	<ul style="list-style-type: none"> <li>• Estimates microstructural features over large parts</li> <li>• Allows extension of preexisting thermal models.</li> </ul>	<ul style="list-style-type: none"> <li>• Does not provide microstructure for further analysis.</li> <li>• Requires estimation of thermal condition.</li> </ul>

**Table 1.** Comparison of AM microstructure simulation methods.

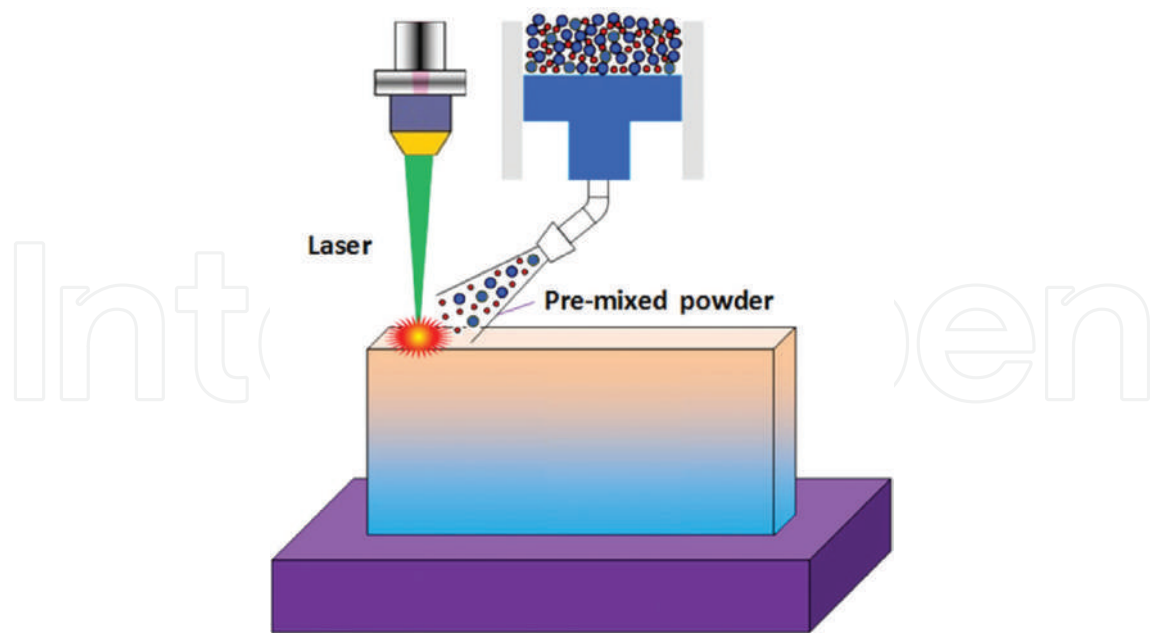


**Figure 1.** Laser powder deposition schematic.

In this study, a predictive multiscale model based on a cellular automaton (CA)-finite element (FE) method has been developed to simulate thermal history and microstructure evolution during metal solidification for a laser-based additive manufacturing process shown in **Figure 1**. ABAQUS was used to calculate the temperature field of the whole part, which offers the macroscopic FE nodes' temperature. In order to integrate the different scales, a coupled model is developed to combine with thermal history and simulate nucleation site, grain growth orientation and rate, epitaxial growth of new grains, remelting of preexisting grains, metal addition and grain competitive growth. Interpolation was utilized to obtain the finer nodes' temperature based on the FE nodes result. The temperature field was validated by the type K thermocouples. The CA model, which was able to show the entrapment of neighboring cells and the relationship between undercooling and the grain growth rate, was built to simulate the microstructure information such as the grain size and columnar grain orientation. The developed "decentered polygon" algorithm is more appropriate for grain structure development in the highly nonuniform temperature field. This simulation will lead to new knowledge that simulates the grain structure development of single- and multiple-layer deposition during DMD process. The microstructure simulation results were validated by the experiment. The model parameters for the simulations were based on Ti-6Al-4V material (**Figure 1**).

## 2. Mathematical model

### 2.1. Ti6Al4V transient temperature field during the deposition process

In the direct metal deposition (DMD) process, the temperature history of the whole domain directly influences the deposition microstructure, which is critical to mechanical properties [28]. In order to obtain the microstructure information during the solidification process, the temperature field must be known at each time step. The transient temperature field throughout

the domain was obtained by solving the 3D heat conduction Eq. (1), in the substrate, along with the appropriate initial and boundary conditions [29].

$$\rho(T) \cdot c_p(T) \cdot \frac{\partial T}{\partial t} = \frac{\partial}{\partial x} \left( k(T) \frac{\partial T}{\partial x} \right) + \frac{\partial}{\partial y} \left( k(T) \frac{\partial T}{\partial y} \right) + \frac{\partial}{\partial z} \left( k(T) \frac{\partial T}{\partial z} \right) + \dot{Q}, \quad (1)$$

where  $T$  is the temperature,  $\rho(T)$  is the density,  $c_p(T)$  is the specific heat,  $k(T)$  is the heat conductivity and  $Q$  is the internal heat generation following certain energy distribution per unit volume.

The initial conditions applied to solve Eq. (1) were:

$$T(x, y, z, 0) = T_0 \text{ and } T(x, y, z, \infty) = T_0, \quad (2)$$

where  $T_0$  is the ambient temperature. In this study,  $T_0$  was set as room temperature, 298 K. The boundary conditions, including thermal convection and radiation, are described by Newton's law of cooling and the Stefan-Boltzmann law, respectively. The laser heating source term,  $\dot{Q}$  in Eq. (1), was also considered in the boundary conditions as a surface heat source. The boundary conditions then could be expressed as [29]

$$K(\Delta T \cdot n)|_{\Gamma} = \begin{cases} [-h(T - T_0) - \varepsilon(T)\sigma(T^4 - T_0^4)]|_{\Gamma} & \Gamma \notin \Lambda \\ [Q - h(T - T_0) - \varepsilon(T)\sigma(T^4 - T_0^4)]|_{\Gamma} & \Gamma \in \Lambda' \end{cases} \quad (3)$$

where  $k$ ,  $T$ ,  $T_0$  and  $Q$  bear their previous definitions,  $n$  is the normal vector of the surface,  $h$  is the heat convection coefficient,  $\varepsilon(T)$  is the emissivity,  $\sigma$  is the Stefan-Boltzmann constant, which is  $5.6704 \times 10^{-8} \text{ W/m}^2 \text{ K}^4$ ,  $\Gamma$  represents the surfaces of the work piece and  $\Lambda$  denotes the surface area irradiated by the Gaussian laser beam.

In order to simulate the thermal history during the direct metal deposition more efficiently and reduce the computational cost, some assumptions were taken into account. In the experiment, a Gaussian distributed laser beam was utilized to melt the substrate vertically with a nonuniform power density [30]. Thus, the transverse intensity variation is described as Eq. (4):

$$I(r, y) = \alpha \frac{P}{\pi w(y)^2/2} \exp\left(-2 \frac{r^2}{w(y)^2}\right), \quad (4)$$

where  $\alpha$  is the laser absorption coefficient,  $P$  is the power of the continuous laser and  $w(y)$  is the distance from the beam axis where the optical intensity drops to  $1/e^2$  ( $\approx 13.5\%$ ) of the value on the beam axis.  $\alpha$  was set as 0.4 based on numerical experiments in the LAMP laboratory and  $w(y)$  is 1 mm in this simulation. The motion of laser beam was simulated by adjusting the position of beam center  $R$  with programming a user subroutine "DFLUX" in ABAQUS. The formula of  $R$  is as follows:

$$R = \left[ \left( x - \int_{t_0}^t u dt \right) + \left( y - \int_{t_0}^t v dt \right) + \left( z - \int_{t_0}^t w dt \right) \right]^{1/2}, \quad (5)$$

where  $x$ ,  $y$  and  $z$  are the spatial coordinates of the Gaussian laser beam center, and  $u$ ,  $v$  and  $w$  are the laser moving velocities.

The Marangoni effect caused by the thermocapillary phenomena can directly influence the temperature field in the whole domain, so it is considered to obtain more accurate thermal history during DMD [31]. The artificial thermal conductivity was put forward to address the Marangoni effect in the finite element method [32]

$$k_m(T) = \begin{cases} k(T), & T \leq T_{liq} \\ 2.5k(T), & T > T_{liq} \end{cases}, \quad (6)$$

where  $k_m$  is the modified thermal conductivity and  $T_{liq}$  is the liquidus temperature.

In the FEA model, the powder addition was simulated by activating elements in many small steps [33]. The width of the deposit area is assumed to be the same as the Gaussian laser beam. The thickness of each layer is calculated by transverse speed, powder feed rate and powder absorption efficiency. The deposit geometry, boundary condition and heat flux were updated after each step.

## 2.2. Ti6Al4V morphology prediction after solidification

Heterogeneous nucleation occurs nearly instantaneously at a characteristic undercooling. The locations and crystallographic orientation of the new nuclei are randomly chosen at the surface or in the liquid. As explained by Oldfield [34], the continuous nucleation distribution,  $dn/d\Delta T'$ , which characterizes the relationship between undercooling and the grain density, is described by a Gaussian distribution both at the mold wall and in the bulk liquid. The parameters of these two distributions, including maximum nucleation density  $n_{max}$ , the mean undercooling  $\Delta T_N$  and the standard deviation of the grain density distribution  $\Delta T_\sigma$ , can be obtained from experiments and grain size measurements. The grain density,  $n(\Delta T)$ , is given by Eq. (7):

$$n(\Delta T) = \int_0^{\Delta T} \frac{dn}{d\Delta T'} d\Delta T' = \int_0^{\Delta T} \frac{n_{max}}{\Delta T_\sigma \sqrt{2\pi}} \exp\left[-\frac{1}{2}\left(\frac{\Delta T' - \Delta T_N}{\Delta T_\sigma}\right)^2\right] d\Delta T', \quad (7)$$

where  $n_{max}$  is the maximum nucleation density of nucleation grains, which is obtained by the integral of the nucleation distribution (from zero undercooling to infinite undercooling).  $\Delta T_N$  and  $\Delta T_\sigma$  are the mean undercooling and standard deviation of the grain density distribution, respectively. Here, all temperatures are in Kelvin.

Undercooling is the most important factor in the columnar and dendrite growth rate and grain size. The total undercooling of the dendritic tip consists of three parts such as solute undercooling, thermal undercooling and curvature undercooling. For most metallic alloys, the kinetic undercooling for atom attachment is small, so it is neglected [35]. The total undercooling can be calculated as follows:

$$\Delta T = m C_0 [1 - A(P_C)] + \theta_t I(P_t) + \frac{2\Gamma}{R}, \quad (8)$$

where  $m$  is the liquidus slope,  $\Gamma$  is the Gibbs-Thomson coefficient,  $C_0$  is the solute concentration in the liquid far from the solid-liquid interface,  $P_t$  and  $P_c$  are the thermal and solutal Peclet numbers, respectively,  $k$  is the solute partition coefficient at the solid-liquid interface,  $A(P)$  equals  $[1 - (1 - k)I(P_c)]^{-1}$ ,  $\theta_t$  is the unit thermal undercooling ( $= \Delta h_f/c$ ) and  $R$  is the radius of the dendritic tip.

For the laser deposition process, the rapid solidification condition corresponds to a high Peclet number at which the dendritic tip radius is given by Eq. (9)

$$R = \left[ \frac{\Gamma}{\sigma^*(m G_c^* - G^*)} \right]^{1/2}, \quad (9)$$

where  $\sigma^*$  is the marginal stability constant, approximately equals  $1/4 \pi^2$  [36], and  $G^*$  and  $G_c^*$  are the effective temperature gradient and concentration gradient, respectively.

### 2.3. Coupling macroscopic FE and mesoscopic CA models

The temperature field result can be used to calculate enthalpy increment, which is necessary to calculate enthalpy at each time step. A linearized implicit FE enthalpy formulation of the heat flow equation can be given [10]

$$\left[ \frac{1}{\Delta t} \cdot [M] + [K]^t \left[ \frac{\partial T}{\partial H} \right]^t \right] \cdot \{\delta H\} = -\{K\}^t \cdot \{T\}^t + \{b\}^t, \quad (10)$$

where  $\{M\}$  is the mass matrix,  $\{K\}$  is the conductivity matrix,  $\{b\}$  is the boundary condition vector and  $\{T\}$  and  $\{H\}$  are the temperature and enthalpy vectors at each node of the FE mesh, respectively. The Newton method and Euler implicit iteration are included in (10). This set of equations can be solved using the Gauss elimination method for  $\{\delta H\}$ .

$$\delta H = \rho \cdot c_p \cdot [T^{t+\delta t} - T^t] - \Delta H_f \cdot \delta f_s. \quad (11)$$

Thus, the next time-step enthalpy can be obtained by the relationship of  $H_i^{t+1} = H_i^t + \delta H$ . The new temperature field can be obtained from the coupling model using (11).  $\Delta H_f$  is the latent heat of fusion per unit volume.  $f_s$  represents the fraction of solid.  $\delta f_s$  can be calculated as in [10].

In the FE macroscopic model, the temperature field was calculated on a relatively coarse mesh, but the solidification microstructure had to be developed on a finer regular CA mesh with a cell size in the order of the secondary dendrite arm spacing (SDAS). **Figure 2** indicates the interpolate relationship between coarse FE nodes and fine CA cells. The known temperature  $T_n^t$  and the volumetric enthalpy variation  $\delta H_n$  were interpolated into the CA network by the linear interpolation in Eqs. (12) and (13).  $\phi_{vn}$  is the interpolation coefficient. Every CA cell temperature in the calculation domain can be obtained with this interpolation.

$$T_v^t = \sum_n \phi_{vn} \cdot T_n^t \quad (12)$$

$$H_v^t = \sum_n \phi_{vn} \cdot H_n^t \quad (13)$$

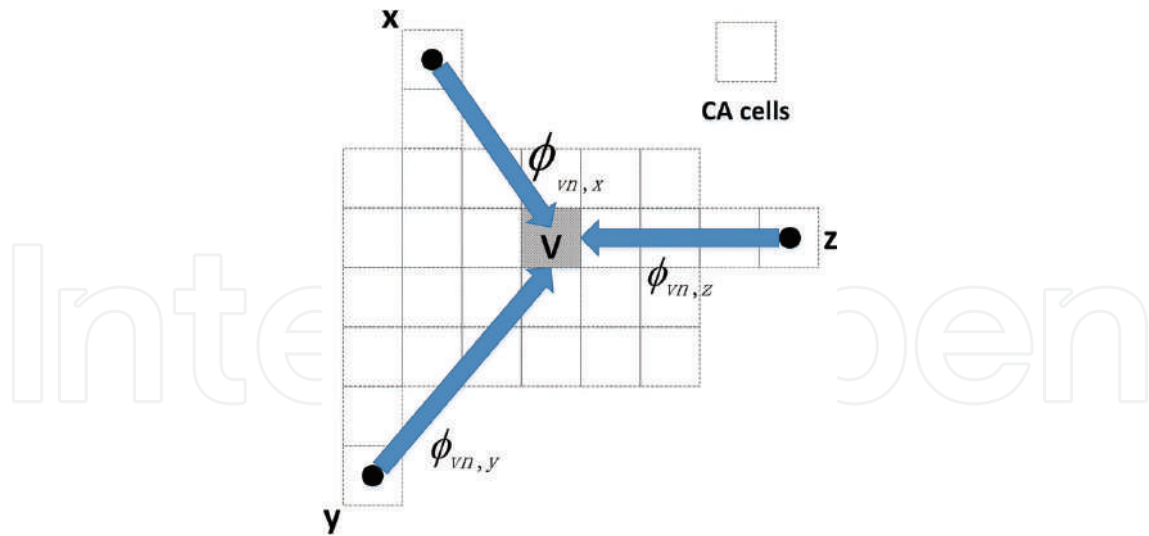


**Figure 2.**  $x$ ,  $y$  and  $z$  represent the FE temperature nodes (coarse grids) and  $v$  represents the CA cells (fine grids). The three linear interpolation coefficients from FE nodes  $x$ ,  $y$  and  $z$  to CA cells  $v$  are  $\phi_{vn,x}$ ,  $\phi_{vn,y}$  and  $\phi_{vn,z}$ .

The finer temperature,  $T_v^t$ , and enthalpy variations,  $\delta H_v^t$ , in regular CA cells were used in Eq. (13) to yield the temperature in the next microtime step. After a few microtime steps, the temperature field in the CA network could be substituted into the coarser nodes of the macroscopic model. The interpolated temperature field is employed as the model input. Heterogeneous nucleation, grain growth orientation and grain growth are solved in the CA-FE model in

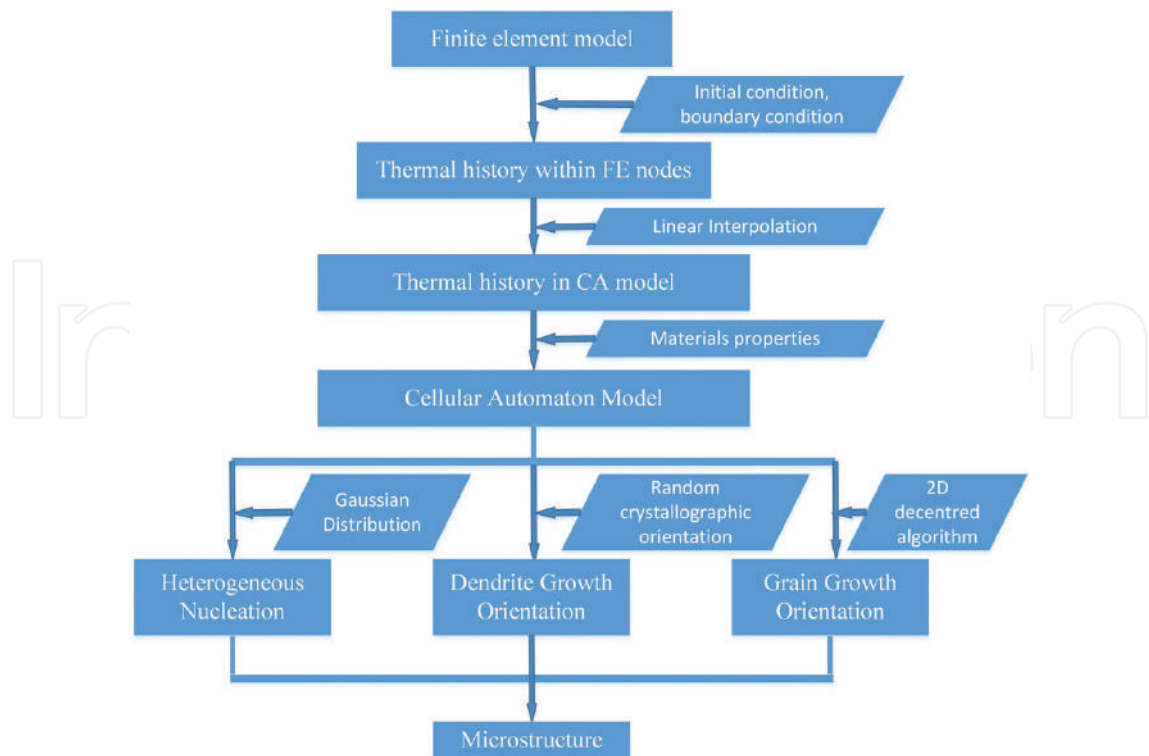


**Figure 3.** Flow chart of the coupling CA-FE model.

terms of nucleation location distribution, random crystallographic orientation and CA cells capture. **Figure 3** indicates the flow chart of coupling FE-CA model. The details of the CA growth algorithm are shown in **Figure 4**.

**Figure 5** illustrates the conventional and modified cell capture algorithm. For the conventional method, the vertices of the square envelope move along the diagonal, and the growth of the square envelope is determined by the center cell temperature, not local temperature, at each time step, which results in the same growth rate for the four vertices. The grain orientation will be along with the axis of computational domain after a few time steps, thus, losing its original orientation information. The modified “decentered polygon” algorithm is implemented to control the grain growth within the melt pool and at the solid/liquid interface. Compared to the traditional “decentered square” algorithm of cell capturing, the modified “decentered polygon” algorithm does not need to create square for each cell when it begins to grow. Only the decentered polygon of a starting nucleated cell is tracked during the grain growth process, which reduces the computational cost. Besides, the modified algorithm can prevent grain orientations from realigning with x axis after a few growing steps because each cell will stop growing when Von Neumann and Moore neighbors are both solid. The controlling point growth rate is determined by the local cell temperature. Therefore, the region with higher thermal gradient will solidify faster along the steepest thermal gradient.

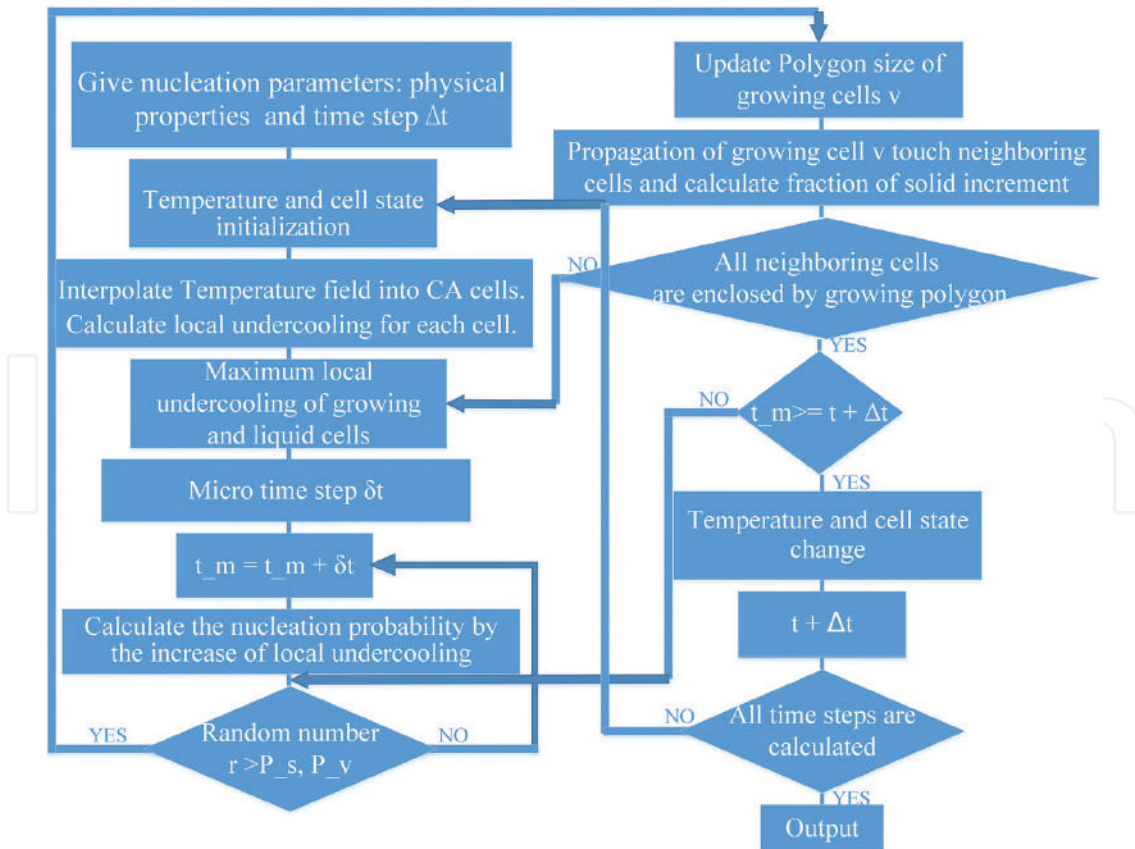


**Figure 4.** Flow chart of CA algorithm.

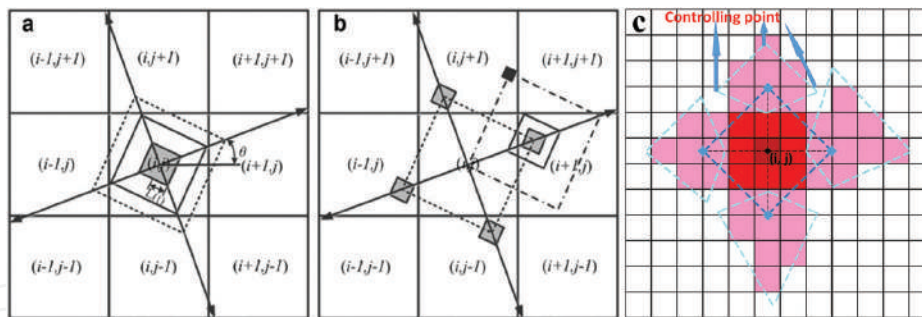


**Figure 5.** Illustration of the conventional and modified cell capture algorithm: (a) capturing rule of cell (i, j) within a decentered square, (b) capturing rule of eight neighboring cells before (i, j) growth termination [37] and (c) the modified cell capture and growth algorithm of “decentered polygon” with neighboring cells effect for cubic crystal alloys.

### 3. Results and discussion

#### 3.1. Single-layer temperature and grain structure

The deposition temperature field and grain morphology were simulated first only in one layer. **Figure 6** shows thermal history of the whole block during the DMD process. **Figure 6(a)** indicates the temperature field of the whole block when laser beam is passing along the x direction at time = 1.0 s, while **Figure 6(b)** shows the temperature field when substrate cools down with laser off at time = 29.0 s. The total physical time of single-layer laser deposition is 2 s, while the cooling time is 28 s in the simulation. For each step, the step time is 0.1 s when the laser is shot on the surface of the deposited material. After 30 s of cooling down, the temperature distribution is more uniform. **Figure 7** indicates the thermal history of two nodes, which locate at the center point in the deposit and 1 mm away from the deposit. The result shows that the highest temperature in the deposit is approximately 2884 K, which occurred at the center of the Gaussian beam. The center node at 1 mm away from the deposit arrives at peak temperature of 1126 K that cannot melt the Ti6Al4V substrate. Based on every node’s thermal history, the undercooling (discrepancy between liquidus temperature and current temperature) that is critical to resulting in grain nucleation and growth rate can be determined.

In order that the input of microstructure model is reliable, the temperature field is validated with four type-K thermocouples. The locations are shown in **Figure 8**. One is located at the starting of laser path, which distance to the laser is approximately 3–3.5 mm. Another three points are located by one side of laser path, which distance to the laser center is approximately 2 mm. Arduino device is used to sample the temperature data. A laser deposition experiment is conducted with the power of 750 W, scanning speed of 600 mm/min and 2 g/min for single-layer deposit. The difference between the experiment and the FEM modeling is less than 10°C shown in **Figure 9**. In **Figure 9(a)**, the delay between the simulated temperature and the thermocouple itself is more visible than **Figure 9(b)–(d)** because the distance of first thermocouple point is further than other three ones. In the real experiment, the substrate is fixed by the metal fixture, which resulting in the more heat conduction than the FEM model. Because of argon gas, forced convection occurred in the real experiment. This also causes lower cooling

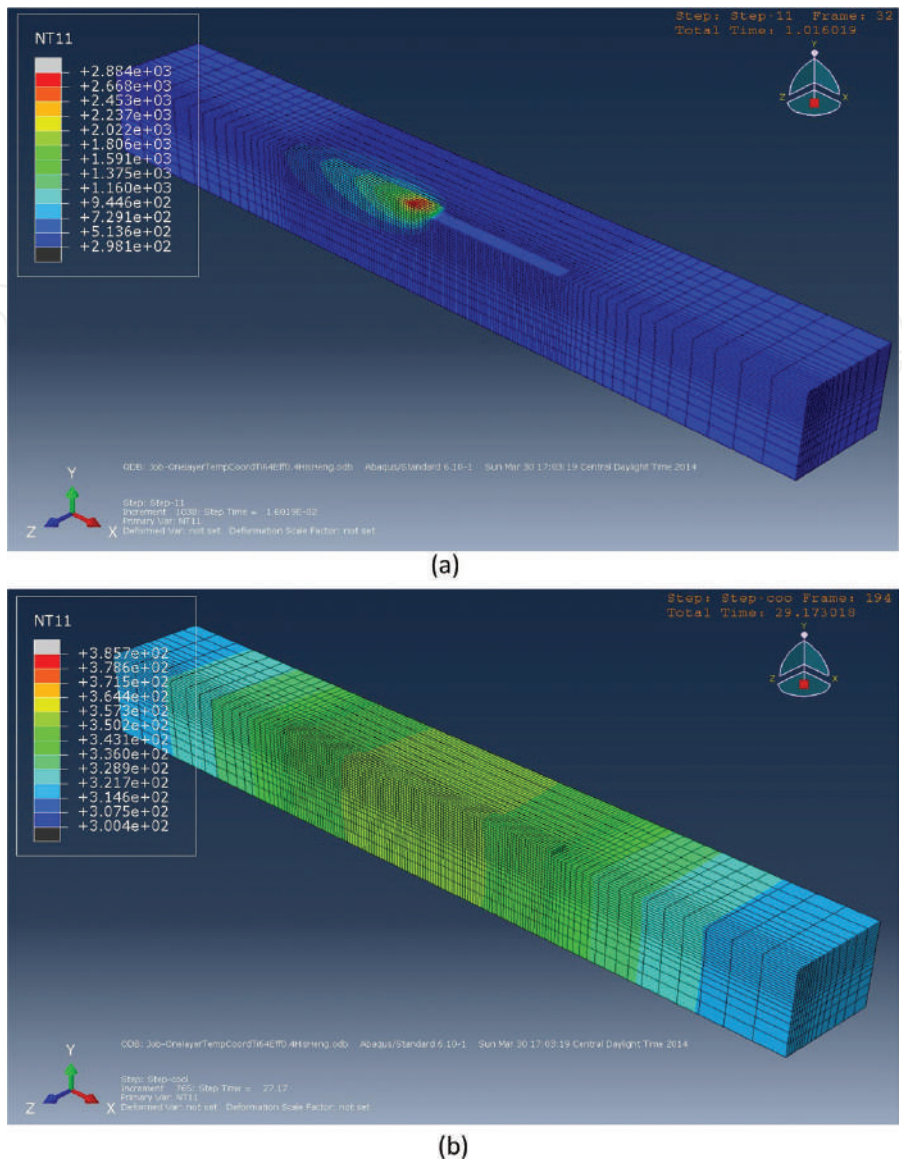


**Figure 6.** Cross-sectional simulated temperature distribution during single-layer laser deposition process. The deposition time is 2 s, while the cooling time is 28 s. (a) Temperature field at time = 1.0 s and (b) temperature field at time = 29.0 s.

rate in the temperature simulation. Because the difference between experiment and simulation is smaller than 10%, the current FEA modeling is still considered as a reasonable simulation of temperature field, which can provide the reliable thermal input for the CA model.

A laser deposition experiment is conducted with the power of 700 W, scanning speed of 600 mm/min and 2 g/min for single-layer deposit. For this case, the cross section shown in the figure is the computational domain. The cell size for this simulation is  $6 \times 6 \mu\text{m}$ . X and Y axes represent the number of cells. The simulation result from conventional method is shown in **Figure 10**. It can be observed that even though different grains own diverse orientation at the very beginning, the crystallographic orientation preference tends to be along with the axis after several time steps. Here, different colors represent various grain orientations. Finally, the equiaxed grains dominate the fusion zone. The original grain orientations are not kept during the solidification process. It does not agree well with the single-layer experimental result shown in **Figure 12**.

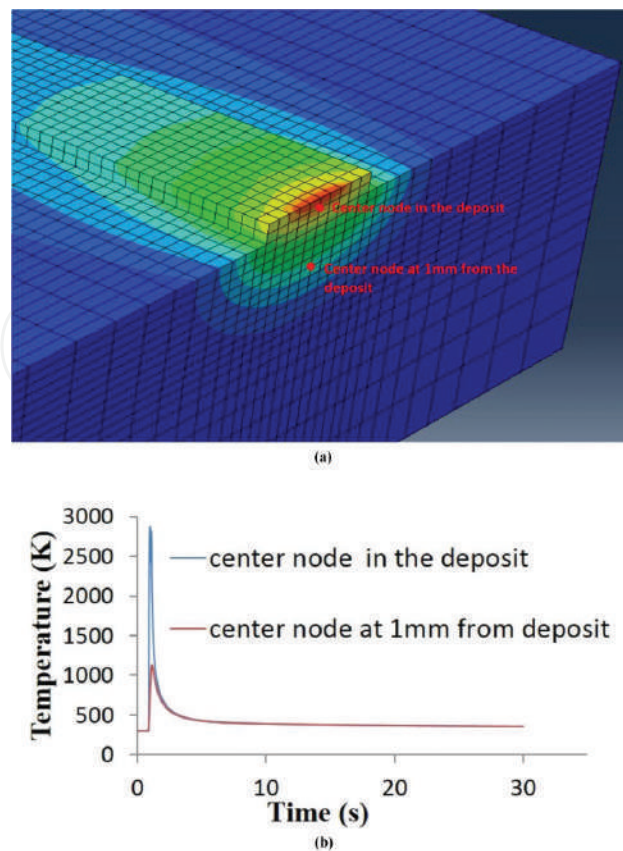


**Figure 7.** (a) Temperature field at  $t = 1$  s (b) Temperature history at the center node in the deposit and substrate.

The developed CA grain growth method is implemented under the same condition. According to the developed CAFÉ simulation, the single layer simulation result is shown in **Figure 11**. The grain keeps its original crystallization orientation when grain growth is modeled. The columnar grain can be identified from the solid/liquid interface. When grains continue to grow toward melt pool center, some grains overgrow other grains such that there are fewer grains further away from the solid/liquid interface.

Three samples of single-layer deposits are prepared with EDM cutting, grinding, polishing and etching. The optical microscope is shown in **Figure 12**. The comparison between simulation and experimental results is shown in **Figure 13**. An average of 20 measurements per sample is performed to determine the average grain size. It compares the experimental aver-

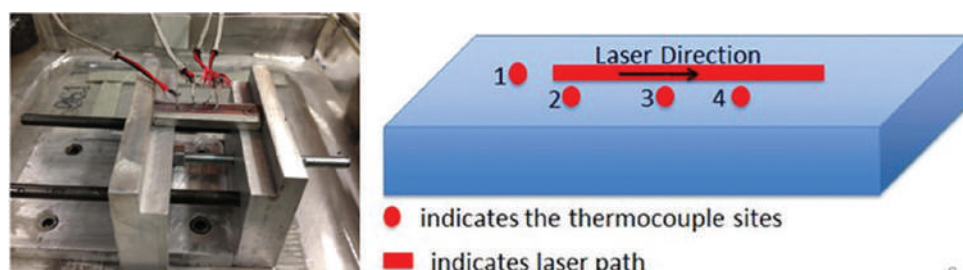


**Figure 8.** Thermocouples location and laser scan direction schematic diagram.

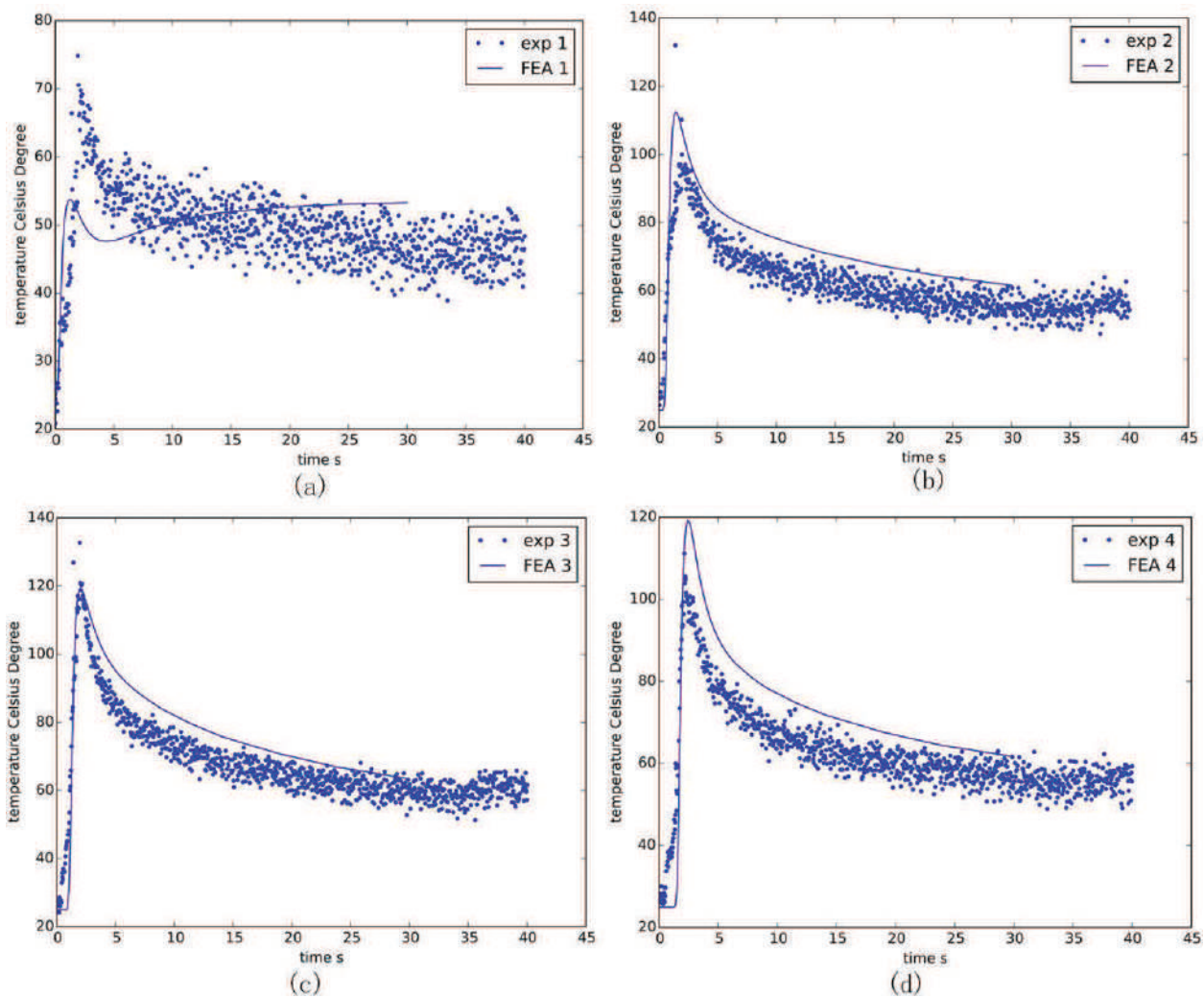


**Figure 9.** Temperature validation with four type-K thermocouples. (a), (b), (c) and (d) are measured at location 1, 2, 3 and 4, respectively.

age grain size with the predicted one. The shown data suggest that a 15% error between experimental measurements and predictions is present. This can be considered as a reasonable prediction of grain morphology and size.

### 3.2. Multilayer temperature and grain structure

**Figure 14** depicts the temperature field of the substrate and deposited material, including the 25-layer deposition materials added on the substrate when the laser is moved forward and backward. The laser deposition of multiple-layer Ti-6Al-4V was conducted with the power of 750 W, scanning speed of 200 mm/min and powder delivery of 2 g/min. The elemental size is nonuniform along the three directions because it is not necessary to apply fine elements to where the location is far from the molten pool. **Figure 15** shows that the thermal history and peak temperature of different layers are not identical. The higher layer performs higher thermal history because the higher layer accumulates more heat than the lower one, and it is closer to heat source.

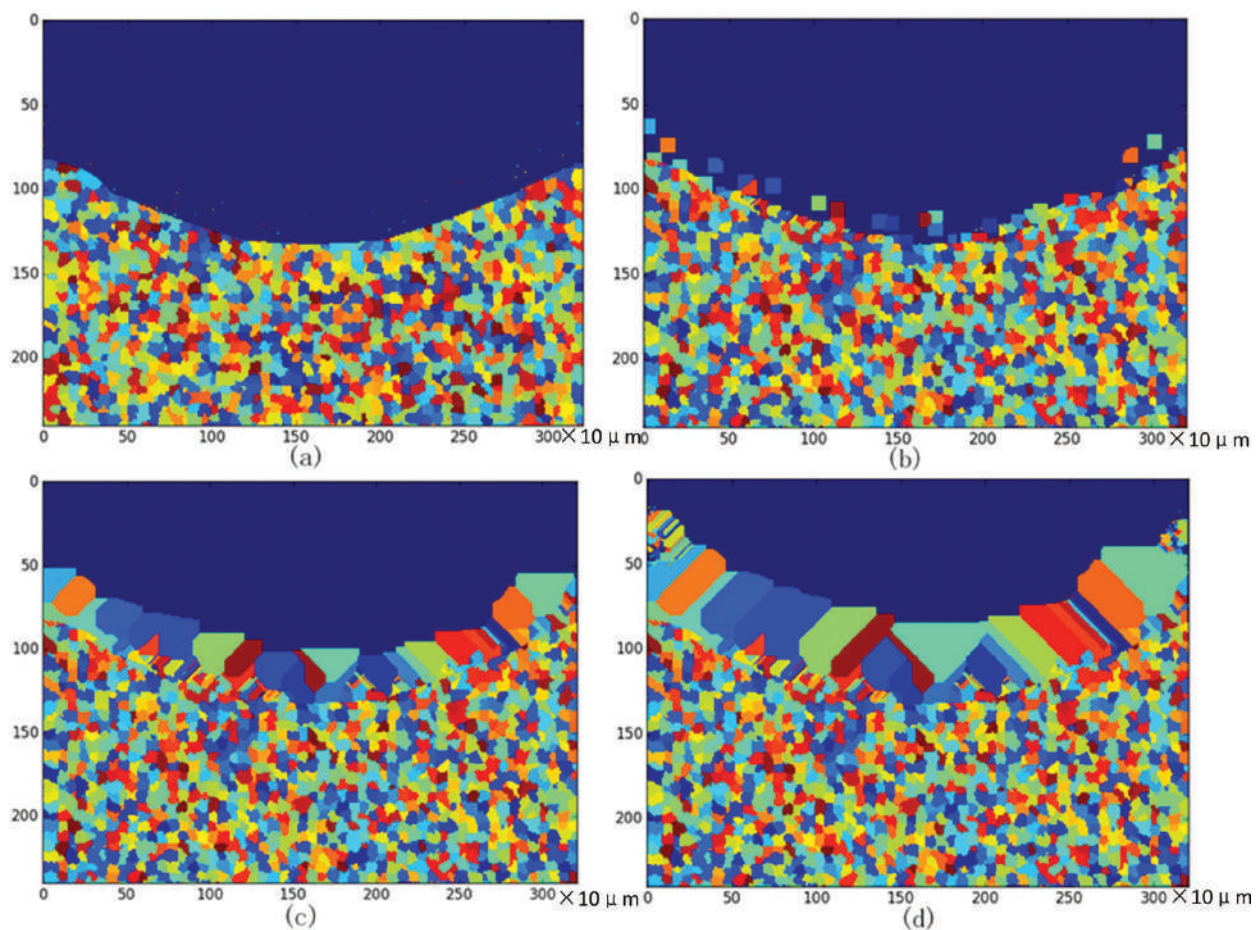


**Figure 10.** Grain structure of conventional growth method for single-layer Ti6Al4V deposition at (a) 5 ms, (b) 25 ms, (c) 45 ms and (d) 65 ms time step.

**Figure 16** shows Ti-6Al-4V deposition grain microstructure. The cross-sectional dimension of deposit region is  $1.8 \times 1.9$  mm, which is close to  $2 \times 2$  mm assumption in the simulation. In **Figure 16**, it can be observed that at the bottom deposition, crystallographic orientation is not only limited to the vertical direction. It can also be observed that columnar grains dominate in the laser deposition area. **Figure 16(a)** and **(b)** indicates the whole deposition region at different magnification and the locations of top and bottom region, while **Figure 16(c)** and **(d)** shows the grain size and shape with higher magnification. Under the same condition, the experiment is conducted, and the optical microscope images are taken. **Figure 16(e)** shows multiple layers of the Ti-6Al-4V grain morphology under the laser deposition process. Irregular grain shape and size can be obtained. When more layers were deposited, prior  $\beta$  columnar grains began to dominate, while equiaxed grains began disappearing. As the solidification process continues, competitive growth among different grains occurs. Therefore, the size of columnar grain increases, and the number of grains goes down. The orientations of the columnar grains were almost perpendicular to the laser motion's direction because the grains grew along the steepest thermal gradient direction. This phenomenon verifies the columnar grain orientation in the simulation result. The domain size in the CA model was  $2 \times 2$  mm. After measurement of grain size, it can be found in **Figure 17** that in the simulation, the grain size ranges from 113 to 346  $\mu$ m. For the

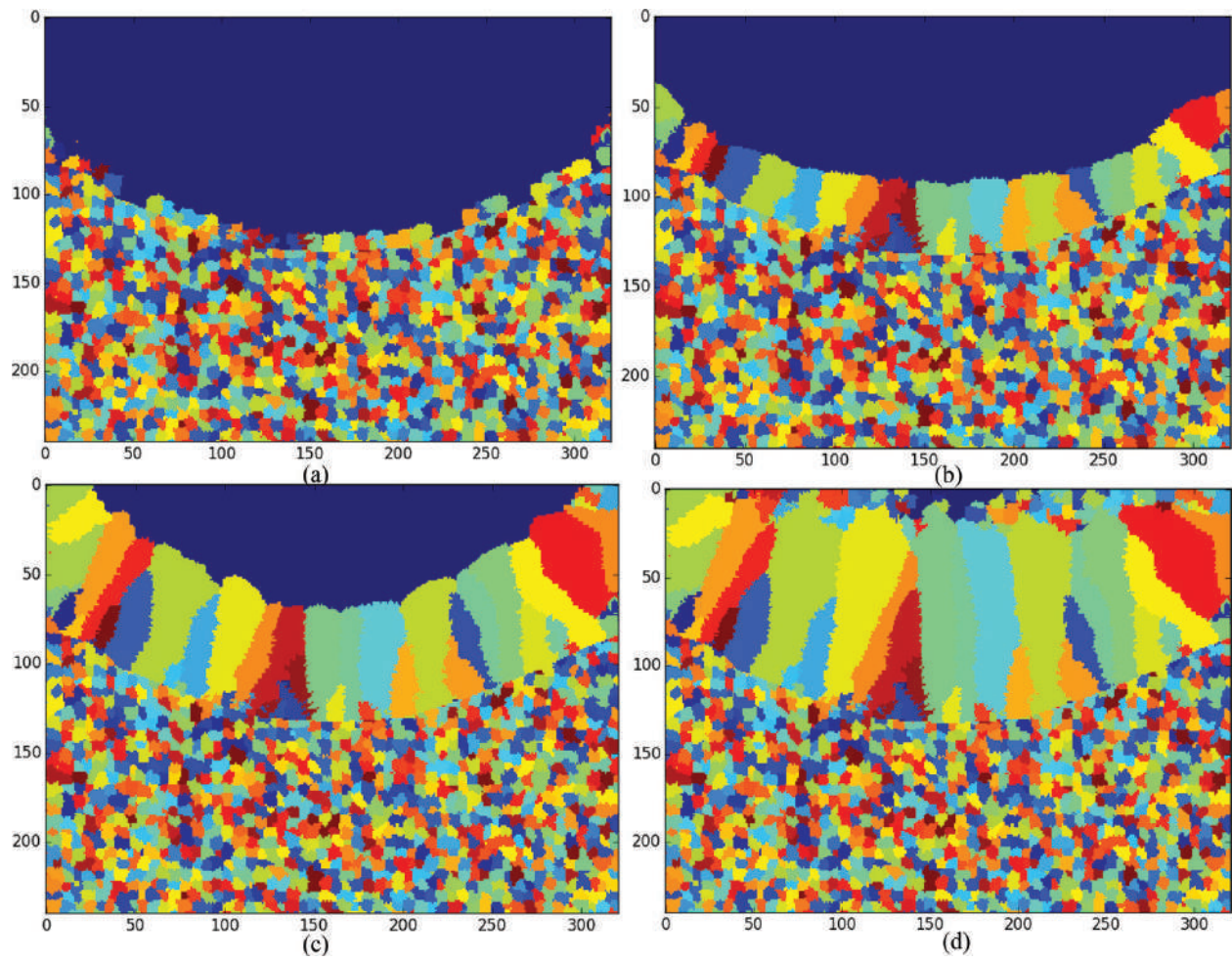


Figure 11. Grain structure of developed growth method for single-layer Ti6Al4V deposition at (a) 20 ms, (b) 40 ms, (c) 60 ms and (d) 80 ms time step.

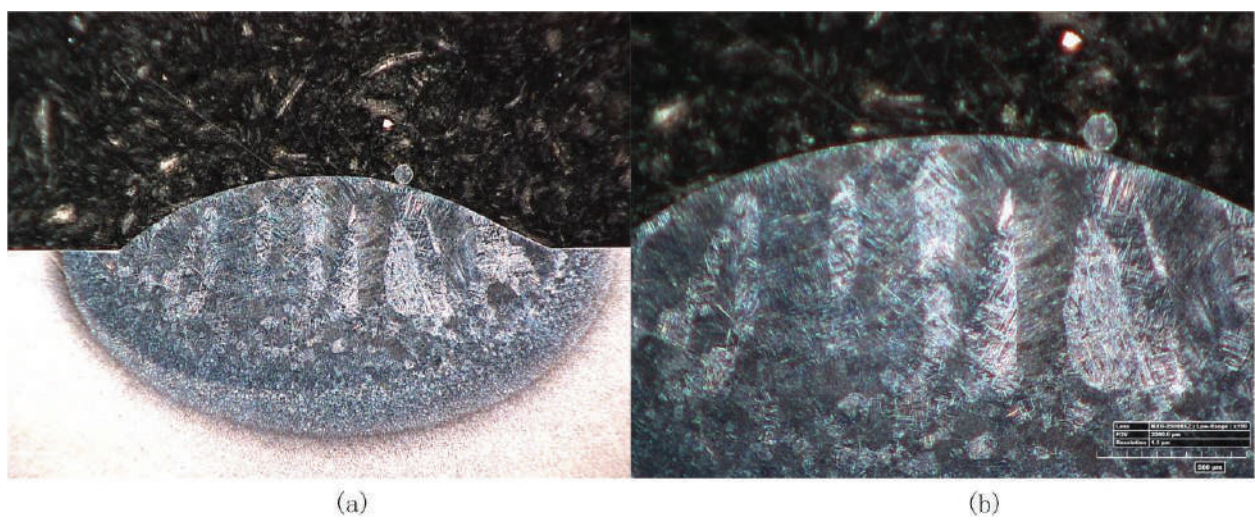


Figure 12. Ti-6Al-4V single-layer deposition grain morphology at (a) 50x and (b) 200x.

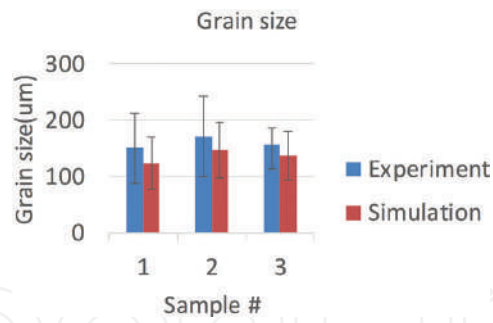


Figure 13. Grain size comparison between simulation and experiment.

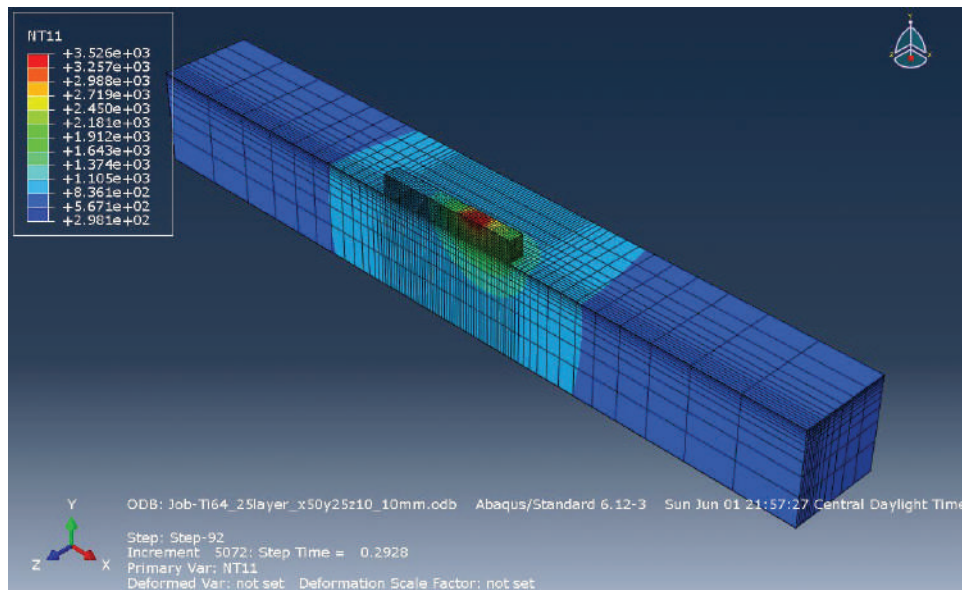


Figure 14. Thermal history for 25-layer Ti-6Al-4V laser deposition. This figure shows the 18th layer deposit temperature field.

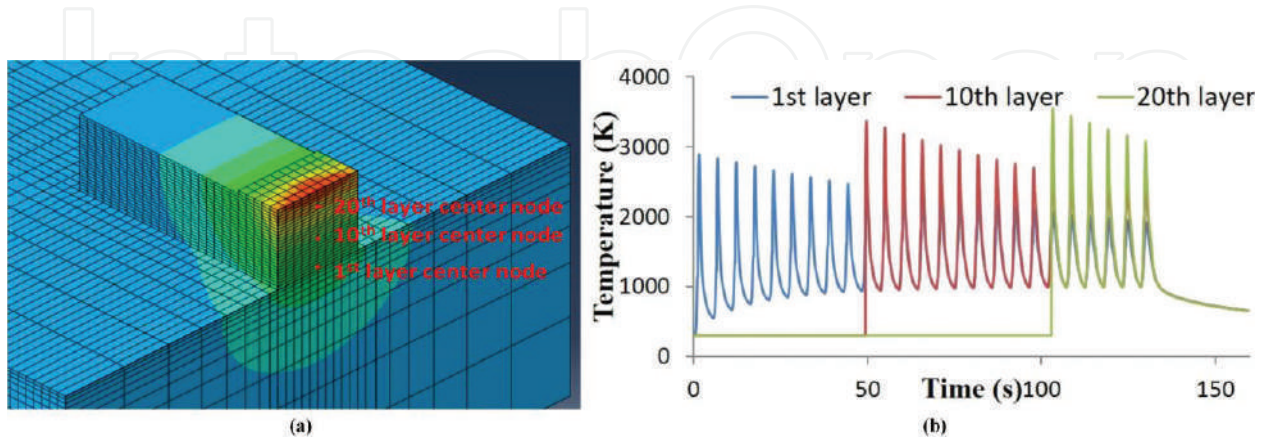
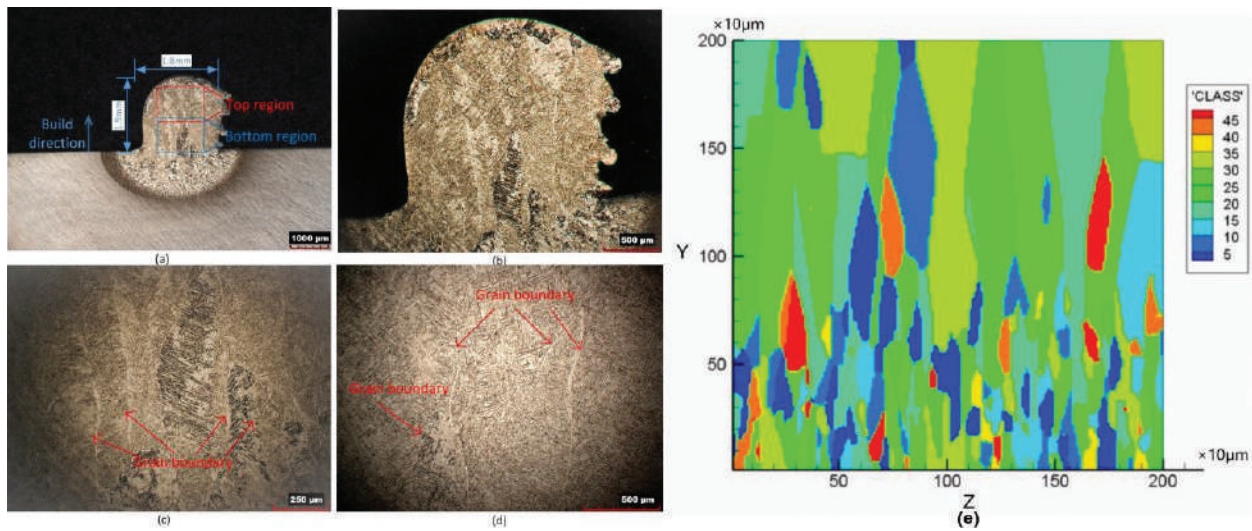
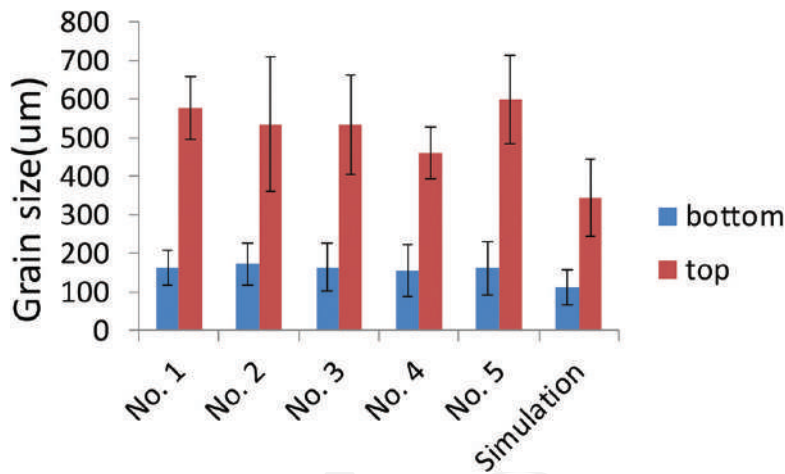


Figure 15. (a) Three nodes location cross section schematic and (b) thermal history of the center node at 1st, 10th and 20th layer.



**Figure 16.** Ti-6Al-4V deposition grain morphologies. (a) and (b) The whole deposition, (c) the bottom region deposition and (d) the top region deposition. (e) Grain morphology modeling of 25-layer Ti-6Al-4V laser deposition. In the legend, “CLASS” represents orientations of different grains. Y and Z coordinates are in agreement with 25-layer thermal history result.



**Figure 17.** Grain size comparison of multiple layers between simulation and experiment.

experiment, the grain size ranges from 156 to 599 μm. The grain size at the bottom and top is larger than the simulation. This may be because it does not consider the cyclic heating and cooling process’ effect on the solidified grain evolution. Usually, cyclic heating will coarsen the grain and make the grain become larger. This effect will be solved in the future research task.

**Figure 18** presents the simulated grain structure from Rai et al. [20] during powder bed additive manufacturing. It can be seen that some grains overgrow others at the top layers, and most surviving grains have negative misorientations indicating grain orientation is aligned well with the beam scanning direction. The detailed local grain boundary misorientation is determined by local thermal gradient and the neighboring grains’ orientation. The rate of overgrowth process also has an effect on the grain boundary angle. Compared to multiple layer results in this investigation, it shows the similarity of grain overgrowth mechanism

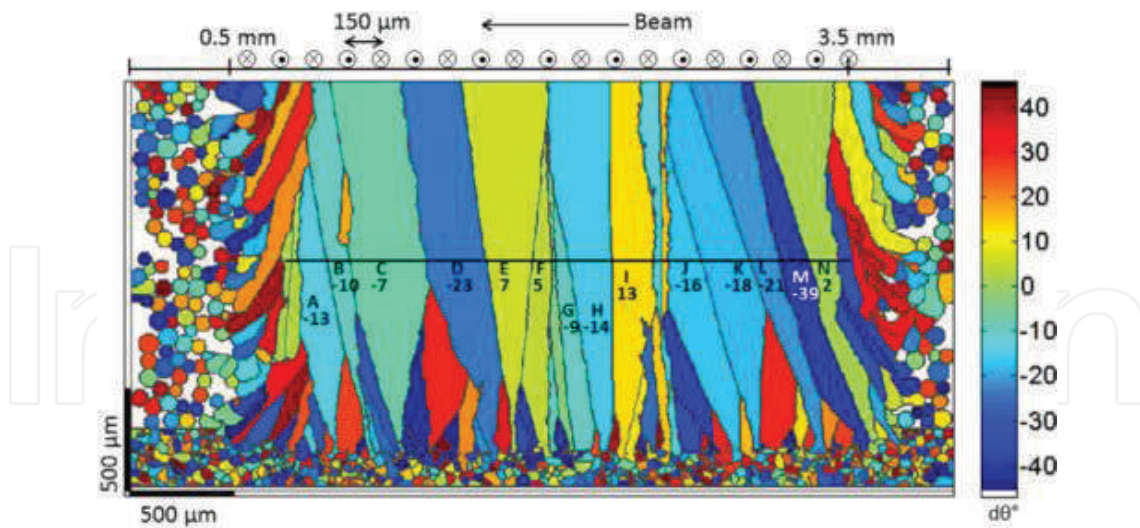


**Figure 18.** Simulated grain structure from Rai et al. [20]. The color bar maps grain misorientation with respect to the build direction.

and misorientation distribution. The grain size between two results is not similar because the thermal gradient and cooling rate are different between powder bed-based additive manufacturing and DMD process.

#### 4. Conclusions

The transient temperature field of single-layer and multiple-layer deposition of Ti-6Al-4V was simulated with finite element method. The simulation result was validated by thermocouple experiment. The FE model provides the temperature at a relatively coarse scale (200 μm), and interpolation algorithm was used to scale the temperature field to match that of the CA model. The FE-CA model predicts grain morphology evolution as the deposition cools down. Hence, the instantaneous nucleation law, grain growth and crystallographic orientation were modeled in this study. It has been found that the developed “decentered polygon” growth method is more appropriate for the highly nonuniform temperature field, and the simulation result is closer to the real experimental measurement compared to the conventional growth method. For multi-layer deposit, columnar grains dominated in the 25-layer deposition in the simulation. The grain size becomes larger when the position is closer to the top area of the deposition, which matches well with the optical microscopic result. The grain size of single and multiple layers between simulation and experiment is similar. It demonstrates that this FE-CA simulation can reasonably predict thermal history and grain morphology during this case of direct metal deposition.

#### Acknowledgements

This work was funded through NASA’s Fundamental Aeronautics Program, Fixed Wing Project, under NRA NNX11AI73A.

## Author details

Jingwei Zhang\*, Lei Yan, Wei Li and Frank Liou

\*Address all correspondence to: jnzp5@mst.edu

Department of Mechanical Engineering, Missouri University of Science and Technology,  
Rolla, MO, United States

## References

- [1] Rappaz M. Modelling of microstructure formation in solidification processes. *International Materials Reviews*. 1989;**34**(3):93-124
- [2] Anderson M, Srolovitz D, Grest G, Sahni P. Computer simulation of grain growth—I. Kinetics. *Acta Metallurgica*. 1984;**32**(5):783-791
- [3] Srolovitz DJ, Anderson MP, Sahni PS, Grest GS. Computer simulation of grain growth—II. Grain size distribution, topology, and local dynamics. *Acta Metallurgica*. 1984;**32**(5):793-802
- [4] Saito Y, Enomoto M. Monte Carlo simulation of grain growth. *ISIJ International*. 1992;**32**(3):267-274
- [5] Chen L-Q. Phase-field models for microstructure evolution. *Annual Review of Materials Research*. 2002;**32**:113-140
- [6] Krill CE III, Chen L-Q. Computer simulation of 3-D grain growth using a phase-field model. *Acta Materialia*. 2002;**50**(12):3059-3075
- [7] Böttger B, Eiken J, Steinbach I. Phase field simulation of equiaxed solidification in technical alloys. *Acta Materialia*. 2006;**54**(10):2697-2704
- [8] Moelans N, Blanpain B, Wollants P. An introduction to phase-field modeling of microstructure evolution. *Calphad*. 2008;**32**(2):268-294
- [9] Rappaz M, Gandin C-A. Probabilistic modelling of microstructure formation in solidification processes. *Acta Metallurgica et Materialia*. 1993;**41**(2):345-360
- [10] Gandin C-A, Rappaz M. A coupled finite element-cellular automaton model for the prediction of dendritic grain structures in solidification processes. *Acta Metallurgica et Materialia*. 1994;**42**(7):2233-2246
- [11] Gandin C-A, Desbiolles J-L, Rappaz M, Thevoz P. A three-dimensional cellular automation-finite element model for the prediction of solidification grain structures. *Metallurgical and Materials Transactions A: Physical Metallurgy and Materials Science*. 1999;**30**(12):3153-3165

- [12] Choudhury A, Reuther K, Wesner E, August A, Nestler B, Rettenmayr M. Comparison of phase-field and cellular automaton models for dendritic solidification in Al–Cu alloy. *Computational Materials Science*. 2012;**55**:263-268
- [13] Dore X. Modelling of microsegregation in ternary alloys: Application to the solidification of Al–Mg–Si. *Acta Materialia*. 2000;**48**:3951-3962
- [14] Jarvis DJ, Brown SGR, Spittle JA. Modelling of non-equilibrium solidification in ternary alloys: Comparison of 1D, 2D, and 3D cellular automaton finite difference simulations. *Materials Science and Technology*. 2000;**16**(December):2-6
- [15] Grujicic M, Cao G, Figliola RS. Computer simulations of the evolution of solidification microstructure in the LENS TM rapid fabrication process. *Applied Surface Science*. 2001;**183**:43-57
- [16] Kelly SM, Kampe SL. Microstructural evolution in laser-deposited multilayer Ti-6Al-4V builds: Part II. Thermal modeling. *Metallurgical and Materials Transactions A: Physical Metallurgy and Materials Science*. 2004;**35**(6):1869-1879
- [17] Kelly SM, Kampe SL. Microstructural evolution in laser-deposited multilayer Ti-6Al-4V builds: Part I. Microstructural characterization. *Metallurgical and Materials Transactions A: Physical Metallurgy and Materials Science*. 2004;**35**(6):1861-1867
- [18] Nie P, Ojo OA, Li Z. Numerical modeling of microstructure evolution during laser additive manufacturing of a nickel-based superalloy. *Acta Materialia*. 2014;**77**(Supplement C): 85-95
- [19] Rodgers TM, Madison JD, Tikare V, Maguire MC. Predicting mesoscale microstructural evolution in electron beam welding. *JOM*. 2016;**68**(5):1419-1426
- [20] Rai A, Helmer H, Körner C. Simulation of grain structure evolution during powder bed based additive manufacturing. *Additive Manufacturing*. 2017;**13**(Supplement C):124-134
- [21] Keller T, Lindwall G, Ghosh S, Ma L, Lane BM, Zhang F, Kattner UR, Lass EA, Heigel JC, Idell Y, Williams ME, Allen AJ, Guyer JE, Levine LE. Application of finite element, phase-field, and CALPHAD-based methods to additive manufacturing of Ni-based superalloys. *Acta Materialia*. 2017;**139**(Supplement C):244-253
- [22] Guo S, Wang M, Zhao Z, Zhang YY, Lin X, Huang WD. Molecular dynamics simulation on the micro-structural evolution in heat-affected zone during the preparation of bulk metallic glasses with selective laser melting. *Journal of Alloys and Compounds*. 2017;**697**:443-449
- [23] Militzer M. Phase field modeling of microstructure evolution in steels. *Current Opinion in Solid State & Materials Science*. 2011;**15**(3):106-115
- [24] Wolf-Gladrow DA. *Lattice-Gas Cellular Automata and Lattice Boltzmann Models*. Springer Berlin Heidelberg; 2000

- [25] Zhou JG. A lattice Boltzmann method for solute transport. *International Journal for Numerical Methods in Fluids*. 2009;**61**(8):848-863
- [26] Rai A, Markl M, Körner C. A coupled Cellular Automaton–Lattice Boltzmann model for grain structure simulation during additive manufacturing. *Computational Materials Science*. 2016;**124**:37-48
- [27] Yin H, Felicelli SD, Wang L. Simulation of a dendritic microstructure with the lattice Boltzmann and cellular automaton methods. *Acta Materialia*. 2011;**59**(8):3124-3136
- [28] Lütjering G. Influence of processing on microstructure and mechanical properties of ( $\alpha+\beta$ ) titanium alloys. *Materials Science and Engineering A*. 1998;**243**(1-2):32-45
- [29] Reddy JN, Gartling DK. *The Finite Element Method in Heat Transfer and Fluid Dynamics*. New York: CRC Press; 2010. p. 39
- [30] Andrews LC, Phillips RL. *Laser Beam Propagation through Random Media*. London: SPIE Publications; 2005. pp. 121-123
- [31] Alimardani M, Toyserkani E, Huissoon JP. A 3D dynamic numerical approach for temperature and thermal stress distributions in multilayer laser solid freeform fabrication process. *Optics and Lasers in Engineering*. 2007;**45**(12):1115-1130
- [32] Lampa C, Kaplan AFH, Powell J, Magnusson C. An analytical thermodynamic model of laser welding. *Journal of Physics D: Applied Physics*. 1997;**30**(9):1293
- [33] Liu H, Sparks T. Modeling and verification of temperature distribution and residual stress in laser aided metal deposition process. *Proceedings of the 6th Annual ISC Graduate Research Symposium*. 2012;(1):1-7
- [34] Oldfield W. A quantitative approach to casting solidification: Freezing of cast iron. *Transactions of American Society for Metals*. 1966;**59**:945
- [35] Fisher DJ, Kurz W. Appendix 7 and 8, *Fundamentals of Solidification*. Aedermannsdorf: Trans Tech Publication Ltd; 1992. pp. 226-246
- [36] Fisher DJ, Kurz W. Appendix 9, *Fundamentals of Solidification*. Aedermannsdorf: Trans Tech Publication; 1992. pp. 247-260
- [37] Chen R, Xu Q, Liu B. A modified cellular automaton model for the quantitative prediction of equiaxed and columnar dendritic growth. *Journal of Materials Science and Technology*. 2014;**30**(12):1311-1320